Air Force Institute of Technology

AFIT Scholar

3-2000

Multi-Conjugate Adaptive Optics for the Compensation of Amplitude and Phase Distortions

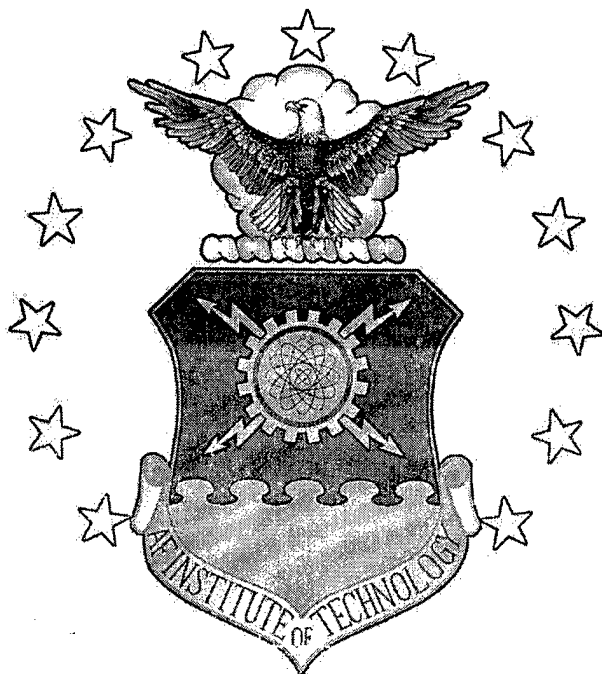Peter N. Crabtree

Follow this and additional works at: https://scholar.afit.edu/etd

 Part of the Optics Commons

Recommended Citation

MULTI-CONJUGATE ADAPTIVE OPTICS FOR THE COMPENSATION OF AMPLITUDE AND PHASE DISTORTIONS

THESIS

PETER N. CRABTREE, CAPTAIN, USAF

AFIT/GEO/ENG/00M-01

DEPARTMENT OF THE AIR FORCE
AIR UNIVERSITY

AIR FORCE INSTITUTE OF TECHNOLOGY

Wright-Patterson Air Force Base, Ohio

The views expressed in this thesis are those of the author and do not reflect the official policy or position of the United States Air Force, Department of Defense, or the U. S. Government.

MULTI-CONJUGATE ADAPTIVE OPTICS FOR THE COMPENSATION OF
AMPLITUDE AND PHASE DISTORTIONS

THESIS

Presented to the Faculty

Department of Electrical Engineering

Graduate School of Engineering and Management

Air Force Institute of Technology

Air University

Air Education and Training Command

In Partial Fulfillment of the Requirements for the

Degree of Master of Science in Electrical Engineering

Peter N. Crabtree, B.S.E.E.

Captain, USAF

March, 2000

MULTI-CONJUGATE ADAPTIVE OPTICS FOR THE COMPENSATION OF
AMPLITUDE AND PHASE DISTORTIONS

Peter N. Crabtree, B.S.E.E
Captain, USAF

Approved:

Dr. Steven C. Gustafson
Chairman, Advisory Committee

6 Mar 00
Date

Major Eric P. Magee
Member, Advisory Committee

6 MAR 2000
Date

Dr. Byron M. Welsh
Member, Advisory Committee

6 March 2000
Date

Acknowledgements

First and foremost I would like to thank my parents for the emphasis they have always placed on education. After setting aside her personal career ambitions years ago to raise my three younger siblings and I, my mother recently graduated with her bachelor's and master's degrees. The utterly sincere appreciation she has for education and the tenacity with which she pursued the completion of her Master's of Teacher Education (MTE) in preparation for work in the classroom has been a true inspiration for me. I would also like to thank my faculty advisors, Dr. Steven Gustafson and Maj Eric Magee, for their guidance and support throughout the course of this thesis effort. Last, but certainly not least, I would like to thank several personnel from the Starfire Optical Range, Kirtland AFB, NM, which sponsored this thesis effort, including Maj David Lee, Capt Jeff Barchers, and Dr. Troy Rhoadarmer.

<div style="text-align: right;">

Peter N. Crabtree

</div>

Table of Contents

List of Figures

List of Tables

Abstract

Two deformable mirrors with finite conjugate ranges are investigated for compensating amplitude and phase distortions due to laser propagation through turbulent atmospheres. Simulations are performed based on Adaptive Optics (AO) for an Airborne Laser (ABL)-type scenario.

The Strehl ratio, the number of branch points in deformable mirror (DM) controls, and the number of iterations to convergence are used as figures of merit to evaluate performance of the Sequential Generalized Projection Algorithm (SGPA) that generates mirror commands. The Strehl ratio and the number of branch points are plotted versus the log-amplitude variance (also known as the Rytov parameter), the conjugate range of the second deformable mirror, and the radii of the deformable mirrors. Also, the number of iterations is plotted versus the Rytov parameter and the conjugate range of the second deformable mirror. The results are ensemble averages over 32 realizations of the scintillated test fields for each value of the Rytov parameter within the test scenario.

The Gaussian beam shape that optimizes the Strehl ratio is determined. The least squares two-DM Strehl, phase-only Strehl, least squares phase-only Strehl, and uncompensated Strehl are also determined for comparison. Finally, for the Strehl ratio versus Rytov parameter analysis the Strehl is also calculated beyond the telescope by propagating the pre-compensated laser wavefront back through the phase screens of the modeled atmosphere.

A conclusion is that an AO transmission system with two DMs clearly improves theoretical performance (compared to a system with one DM) in delivering energy on

target through atmospheric turbulence. Also, placing the second DM at a finite conjugate range minimizes energy lost outside the radius of the first deformable mirror and thus maximizes the Strehl ratio. Finally, it is also concluded that hidden phase contained in the branch points is critical to the performance of the SGPA algorithm. It is suggested that non-least squares methods and/or branch point number constraints could reduce hidden phase effects to further improve performance.

MULTI-CONJUGATE ADAPTIVE OPTICS FOR THE COMPENSATION OF AMPLITUDE AND PHASE DISTORTIONS

1. Introduction

A majority of Adaptive Optics (AO) research to date has focused on phase-only correction systems, where the primary goal is the improved imaging of space objects at observation angles near zenith. For laser communications or high-energy weapon systems such as the Airborne Laser (ABL), however, AO must also provide correction for scintillation in the amplitude of the transmitted field. This thesis explores the two-deformable mirror (DM), multi-conjugate configuration applied to full optic conjugation in order to correct for both phase and amplitude distortions in the transmitted beam.

1.1 Problem Statement

High quality telescope mirrors as large as 10 meters are available, but typically they can provide angular resolution no better than that of a 25 cm telescope at optical wavelengths due to atmospheric turbulence. The Hubble Space Telescope (HST) is one solution to this problem but is very expensive. Another solution is adaptive optics [1].

Adaptive optics systems can be broadly divided into two basic types, those designed for transmission and those designed for imaging. Examples of transmitting systems are tactical communications and high-energy laser weapons (e.g., ABL). Imaging systems are used mainly for astronomy or ground-based satellite surveillance.

Common to all AO systems, however, are the performance-hindering effects of atmospheric turbulence.

For transmission systems, turbulence can result in degradation of the signal to noise ratio or in a decrease in energy on target. The goal addressed in this thesis is the evaluation of a deformable mirror control algorithm for a Multi-Conjugate Adaptive Optics (MCAO) system designed to compensate for strong turbulence due to propagation over long horizontal paths, where the second deformable mirror is conjugate to a finite distance from the telescope's collecting aperture.

1.2 Document Organization

Chapter two summarizes various background theories on which this research is based. Chapter three introduces the Fourier-transform-based phase screen generation method used to model atmospheric turbulence. Layered models together with a wave propagation algorithm are used to create test fields with varying degrees of scintillation in the amplitude profile. Statistics of both the individual phase screens and the scintillated test fields are calculated and compared with theory. Chapter four develops the algorithm used to obtain the deformable mirror commands and describes branch points and least squares reconstruction. Chapter five presents and discusses key results. Finally, chapter six summarizes the research effort and provides recommendations for further research.

2. Background

2.1 Adaptive Optics

It has long been known that the turbulence in the atmosphere distorts images of heavenly bodies as seen from earth. Operation of a single deformable mirror AO imaging system to compensate for these distortions is conceptually quite simple. Light from a distant point source is essentially a plane wave as it enters the earth's atmosphere. Propagating downward through the atmosphere, a spatially coherent planar wave encounters pockets of air that vary in temperature and therefore density, resulting in slight variations in refractive index. Different portions of the wavefront are thus subject to slightly different optical path lengths between the top of the atmosphere and the collecting aperture of a telescope.

The distorted wavefront arriving at the telescope is often described as being wrinkled. These wrinkles, or distortions, can be monitored in real time by wavefront sensors. Popular designs include the Shack-Hartmann wavefront sensor and the shearing interferometer. Imaging the pupil plane of the telescope onto a deformable mirror that is controlled on a millisecond timescale allows these "wrinkles" to be removed, resulting in images of near diffraction-limited quality. A tip-tilt mirror is also normally included in the system to correct for overall tilt in the distorted wavefront, thus removing what appears as jitter to the human eye.

2.1.1 Brief History

Like many other ideas that were realized for the first time in the twentieth century due to technological/manufacturing advances, Adaptive Optics is not particularly new.

Horace Babcock was apparently the first to suggest, early in the 1950s, a system for improved astronomical imaging. His approach used an electrostatically controlled thin layer of oil to introduce corrective phase delays. In 1957, a Russian, Vladimir P. Linnik, independently described the same concept in a Soviet Journal. Several decades later, when the space programs of Russian and the U.S. were in full swing, the DOD took the lead in advancing AO technology. The first fully operational adaptive optics system was built and installed in a surveillance telescope at Haleakala Observatory on Maui, Hawaii, for the purpose of imaging Russian satellites launched during the cold war [1].

2.1.2 Single Deformable Mirror System

A basic system diagram of a single deformable-mirror AO system applied to imaging is shown below in Figure 2.1. The incoming distorted wavefront is captured by the primary mirror, re-imaged onto the deformable mirror, and then passed on to a wavefront sensor. The Shack-Hartmann sensor actually measures wavefront slopes over an array of sub-apertures. This slope data is passed to a computer that employs an algorithm (such as least squares) to reconstruct the phase from the slopes, which is then used to provide control commands to the deformable mirror. The wavefront sensor is normally placed "downstream" from the deformable mirror so that the system can perform as a closed-loop control system. For observations near zenith the sensed wavefront contains primarily phase-only distortions, and thus near diffraction-limited results may be obtained.

Incoming Beacon Field
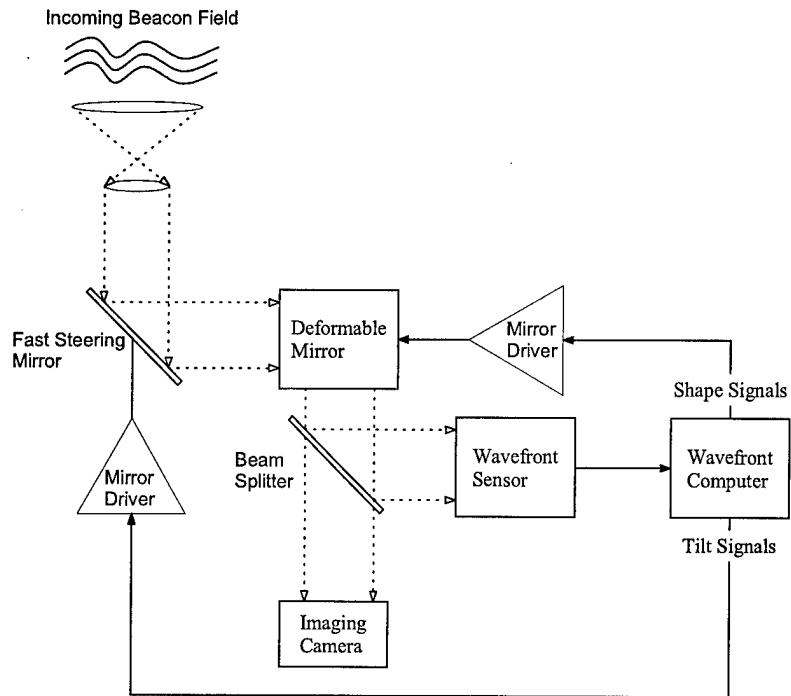
Figure 2.1. Block Diagram for a Single Deformable Mirror Imaging System

2.1.3 Two Deformable Mirror System

The addition of a second deformable mirror to a transmitting system as shown in

Figure 2.2 allows pursuit of full optic conjugation. Such conjugation is achieved by

taking advantage of the fact that phase modulation followed by propagation results in

changes to the light wave amplitude. By employing a deconvolution type algorithm, the

second deformable mirror can be driven to a shape that results in an amplitude field equal

to that of the sensed field after propagation of a laser from DM2 to DM1. A two-DM AO

system with the second deformable mirror conjugate to infinity (i.e., the far-field) was

previously studied by Roggemann and shown to provide an increase in on-target on-axis

2-3

light field amplitude by a factor of 1.4 to 1.5 as compared with a one-DM phase-only

correction system [2].
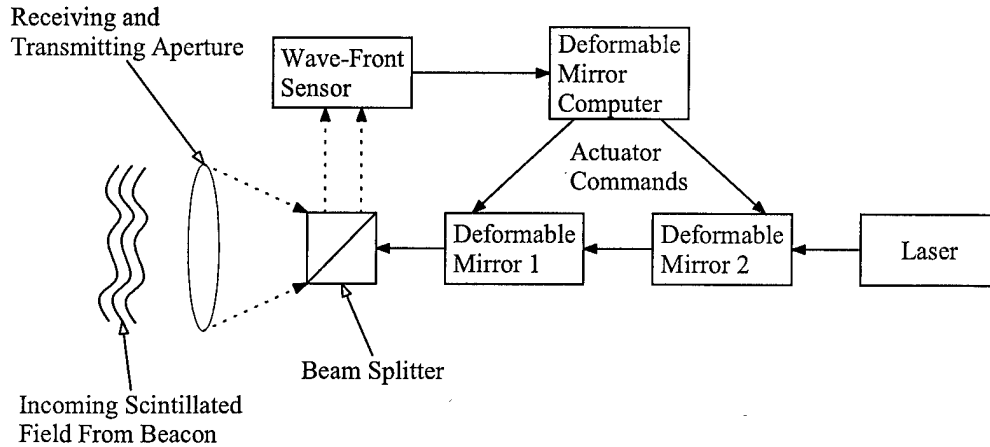
Figure 2.2. Block Diagram for a Two Deformable Mirror Transmission System

2.1.4 Figures of Merit

One of the primary metrics used to assess the performance of adaptive optics

systems is the Strehl ratio, which is defined as the on-axis intensity in the far-field

produced by a system with no aberrations divided by the on-axis intensity of the aberrant

system. This ratio is expressed in terms of the incoherent imaging point-spread function

(psf),

$$S = \frac{psf_{with}(0,0)}{psf_{without}(0,0)} \quad , \tag{2.1}$$

where *with* indicates the aberrant system and *without* indicates the diffraction limited system. The amplitude psf describes a coherent imaging system and is simply the Fraunhofer diffraction pattern of the exit pupil,

$$h(u,v) = \frac{A}{\lambda z_i} \int_{-\infty}^{\infty} \int_{-\infty}^{\infty} dx\, dy\, P(x,y) \exp\left\{ -i \frac{2\pi}{\lambda z_i} (ux + vy) \right\} \quad , \tag{2.2}$$

where A is a constant amplitude, λ is the wavelength of light, z_i is the distance between the exit pupil and image planes, $P(x, y)$ describes the shape of the exit pupil, and (x, y) and (u, v) are the coordinates in the exit pupil and image planes, respectively. The amplitude transfer function is simply the Fourier transform of Equation (2.2), which turns out to be simply a scaled version of the pupil function. Because the pupil function is normally symmetric the amplitude transfer function can be expressed as

$$H(f_X, f_Y) = P(\lambda z_i f_X, \lambda z_i f_Y) \quad . \tag{2.3}$$

The Optical Transfer Function (OTF) describes an incoherent imaging system and is the normalized Fourier transform of the squared modulus of the amplitude psf,

$$\mathcal{H}(f_X, f_Y) = \frac{\displaystyle\int_{-\infty}^{\infty}\int_{-\infty}^{\infty} du\, dv\, |h(u,v)|^2 \exp\left[-j2\pi (f_X u + f_Y v) \right]}{\displaystyle\int_{-\infty}^{\infty}\int_{-\infty}^{\infty} du\, dv\, |h(u,v)|^2} \quad . \tag{2.4}$$

With the help of Rayleigh's theorem, the OTF can also be expressed as the normalized autocorrelation function of the amplitude transfer function

$$\mathcal{H}(f_X, f_Y) = \frac{\displaystyle\int_{-\infty}^{\infty}\int_{-\infty}^{\infty} dx\, dy\, P\left(x + \frac{\lambda z_i f_X}{2}, y + \frac{\lambda z_i f_Y}{2} \right) P^*\left(x - \frac{\lambda z_i f_X}{2}, y - \frac{\lambda z_i f_Y}{2} \right)}{\displaystyle\int_{-\infty}^{\infty}\int_{-\infty}^{\infty} dx\, dy\, |P(x,y)|^2} \tag{2.5}$$

For an aberrant system the psf is calculated in the same fashion after replacing $P(x, y)$ with a generalized pupil function given by

$$\mathcal{P}(x, y) = P(x, y) \exp\left[ikW(x, y)\right] \quad , \qquad (2.6)$$

where $W(x, y)$ describes the remaining aberrations present in the system after adaptive optics compensation. The OTF describing an aberrant system is thus

$$\mathcal{H}(f_X, f_Y) = \frac{\mathcal{P}(\lambda z_i f_X, \lambda z_i f_Y) \star \mathcal{P}^*(\lambda z_i f_X, \lambda z_i f_Y)}{\mathcal{P}(0,0) \star \mathcal{P}^*(0,0)} \qquad (2.7)$$

The psf describing an incoherent imaging system can now be expressed as the inverse Fourier transform of the OTF given by Equation (2.7),

$$psf(x, y) = \mathcal{F}^{-1}\left\{\mathcal{H}(f_X, f_Y)\right\} \qquad (2.8)$$

where $\mathcal{F}^{-1}$ represents the two-dimensional inverse Fourier transform.

Equation (2.1) can be directly applied to single deformable mirror AO imaging systems, but it must be altered somewhat for application to the 2-DM laser transmission configuration. In order to reverse the effects of turbulence, the outgoing laser wavefront must have an amplitude profile identical to that of the sensed beacon field and a phase profile equal to the conjugate of the sensed wavefront. The far-field on-axis intensity is clearly proportional to the degree to which phase conjugation is successfully accomplished, or

$$I \propto \left| \int dr\, U_0(r) U_b(r) \right|^2 \quad , \qquad (2.9)$$

where $U_0(r) = A_0(r)e^{i\phi_0(r)}$ describes the field of the outgoing laser in the pupil plane and

$U_b(r) = A_b(r)e^{i\phi_b(r)}$ describes the sensed beacon field in the pupil plane. In the best-case

scenario the field of the outgoing laser is

$$U_{0,\text{ideal}}(r) = kA_b(r)e^{-i\phi_b(r)} \quad , \tag{2.10}$$

where k is a constant. The maximum far-field on-axis intensity is now

$$I_{\text{max}} = \left| \int dr\, kA_b(r)A_b(r) \right|^2 = \int dr\, k^2 A_b^{\,2}(r) \int dr'\, A_b^{\,2}(r') \quad . \tag{2.11}$$

The normalized far-field on-axis intensity is then

$$I = \frac{\left| \int dr\, U_0(r)U_b(r) \right|^2}{\left| \int dr\, k^2 A_b^{\,2}(r) \right| \left| \int dr\, A_b^{\,2}(r) \right|} \quad . \tag{2.12}$$

The first factor in the denominator represents the energy contained in the field

transmitted by the laser after modulation by DM2, propagation from DM2 to DM1, and

modulation by DM1. Since the free-space propagation represented by $T_z[\cdot]$ conserves

energy, the first factor in the denominator equals the energy in the original laser field

(assuming no loss from the deformable mirrors), i.e.,

$$Energy_{laser} = \int dr\, U_l(r)U_l^*(r) = \int dr\, A_l^{\,2}(r) \quad . \tag{2.13}$$

Equation (2.12) is finally rewritten as

$$I = \frac{\left| \int dr\, U_0(r)U_b(r) \right|^2}{\left| \int dr\, U_l(r)U_l^*(r) \right| \left| \int dr\, U_b(r)U_b^*(r) \right|} \quad . \tag{2.14}$$

2.2 Propagation of Optical Radiation

2.2.1 Angular Spectrum and the Propagation Transfer Function

The propagation of optical fields through homogeneous media can be formulated to allow the application of linear systems theory, which is an invaluable tool for analysis. A wave traveling in the positive z direction is described in any plane perpendicular to its path by its angular spectrum, which is simply the Fourier transform of the field with direction cosine terms substituted for the spatial frequency variables. This formulation indicates that any field can be described in terms of a weighted sum of plane waves traveling in various directions. If a field is known at $z = 0$, then the effects of propagation through the homogeneous media are described by the transfer function of wave propagation

$$H(f_x,f_y) = \begin{cases} \exp\left[j2\pi \dfrac{z}{\lambda}\sqrt{1-(\lambda f_x)^2 - (\lambda f_y)^2} \right] & \sqrt{f_x^2+f_y^2} < \dfrac{1}{\lambda} \\ 0 & \text{otherwise} \end{cases} , \qquad (2.15)$$

such that the field after traveling a distance z is

$$A(f_x,f_y;z) = A(f_x,f_y;0)H(f_x,f_y) \quad , \qquad (2.16)$$

where $A(f_x,f_y;0)$ is the two-dimensional Fourier transform

$$A(f_x,f_y;0) = \int_{-\infty}^{\infty}\int_{-\infty}^{\infty} dx\, dy\, U(x,y,0)\exp\left[-i2\pi(f_x x + f_y y)\right] \quad , \qquad (2.17)$$

and f_X and f_Y are the spatial frequency variables in the x and y directions, respectively.

2.2.2 Fresnel Approximation to the Angular Spectrum Propagator

A simple method for deriving the Fresnel approximation to the propagation transfer function applies a binomial expansion and approximation to the exponent of Equation (2.15). The binomial expansion of $\sqrt{1-x}$ is

$$1 - \frac{1}{2}x - \frac{1}{8}x^2 - \frac{1}{16}x^3 - \cdots \quad . \tag{2.18}$$

Using the first two terms of the expansion, the exponent is simplified, i.e.,

$$\sqrt{1 - (\lambda f_x)^2 - (\lambda f_y)^2} \approx 1 - \frac{(\lambda f_x)^2}{2} - \frac{(\lambda f_y)^2}{2} \quad . \tag{2.19}$$

The Fresnel approximation to the angular spectrum propagator is thus

$$H(f_x, f_y) = \begin{cases} \exp^{ikz} \exp\left[-i\pi\lambda z \left(f_x^2 + f_y^2\right)\right] & |\lambda f_x| \ll 1 \text{ and } |\lambda f_x| \ll 1 \\ 0 & \text{otherwise} \end{cases} \quad . \tag{2.20}$$

2.3 Statistics and Random Processes

For linear time-invariant (LTI) systems and deterministic signals, the input, $x(t)$, and output, $y(t)$, are related by

$$y(t) = x(t) \otimes h(t) \quad , \tag{2.21}$$

where $h(t)$ is the impulse response of the system and $\otimes$ is the convolution operator. The input-output relation is expressed by straightforward multiplication in the frequency (i.e., Fourier Transform) domain

$$Y(f) = X(f)H(f) \quad , \tag{2.22}$$

where $Y(f)$, $X(f)$, and $H(f)$ are the Fourier transforms of $y(t)$, $x(t)$, and $h(t)$, respectively. Under certain conditions a similar relationship holds for stochastic signals. For Wide Sense Stationary (WSS) random processes, the power spectral density of the input and output of a LTI system are related by

$$S_y(f) = S_x(f)|H(f)|^2 \quad , \qquad (2.23)$$

where $S_x(f)$ and $S_y(f)$ are the power spectra of the input and output, respectively, and $H(f)$ is again the Fourier transform of the system impulse response. Another special relationship exists between the autocorrelation function and power spectral density of a WSS random process:

$$S(f) = \mathcal{F}\{\Gamma(\tau)\} \quad . \qquad (2.24)$$

In general, the spatial autocorrelation function of a real-valued process $\phi(\vec{r})$ is

$$\Gamma_\phi(\vec{r_1}, \vec{r_2}) = E\{\phi(\vec{r_1})\phi(\vec{r_2})\} \quad . \qquad (2.25)$$

Several assumptions greatly simplify this expression. First, if the process is assumed to be homogeneous, then the statistics describing it are independent of location, and the autocorrelation is only a function of the separation vector $\vec{r} = \vec{r_1} - \vec{r_2}$, i.e.,

$$\Gamma_\phi(\vec{r}) = E\{\phi(\vec{r_1})\phi(\vec{r_1} - \vec{r})\} \quad . \qquad (2.26)$$

Second, if the process is also isotropic, then the statistics (i.e., properties of the medium) do not depend on direction, and the autocorrelation is a function only of the magnitude of the separation vector.

Subsequent to propagation through atmospheric turbulence, the variance of an uncompensated distorted wavefront observed in a circular aperture is

$$\sigma^2_{uncomp} = 1.0299 \left(\frac{D}{r_0} \right)^{5/3} \quad , \tag{2.27}$$

where D is the aperture diameter and r_0 is the Fried parameter, which is related to turbulence strength [3]. Subsequent to piston and tilt removal, the variance is

$$\sigma^2_{tiltcomp} = 0.134 \left(\frac{D}{r_0} \right)^{5/3} \quad . \tag{2.28}$$

The corresponding expression for a square aperture is

$$\sigma^2_{tiltcomp} = 0.1748 \left(\frac{L}{r_0} \right)^{5/3} \quad , \tag{2.29}$$

where L is the length of a side of the aperture.

Another statistical quantity used frequently to describe turbulence is the structure function

$$D_\phi \left(\vec{r}_1, \vec{r}_2 \right) = E \left\{ \left[\phi \left(\vec{r}_1 \right) - \phi \left(\vec{r}_2 \right) \right]^2 \right\} \quad . \tag{2.30}$$

For homogeneous media, the structure function is

$$D_\phi \left(\vec{r} \right) = E \left\{ \left[\phi \left(\vec{r}_1 \right) - \phi \left(\vec{r}_1 - \vec{r} \right) \right]^2 \right\} \quad . \tag{2.31}$$

By expanding the argument of the expectation operator, Equation (2.31) can be rewritten as

$$D_\phi \left(\vec{r} \right) = E \left\{ \left[\phi \left(\vec{r}_1 \right)^2 - 2\phi \left(\vec{r}_1 \right) \phi \left(\vec{r}_1 - \vec{r} \right) + \phi \left(\vec{r}_1 - \vec{r} \right)^2 \right] \right\} \quad . \tag{2.32}$$

The homogeneity assumption (i.e., $E \left[\phi^2 \left(\vec{r}_1 \right) \right] = E \left[\phi^2 \left(\vec{r}_2 \right) \right]$) allows further simplification:

2-11

$$D_\phi\left(\overline{r}\right) = 2E\left\{\left[\phi\left(\overline{r_1}\right)^2 - \phi\left(\overline{r_1}\right)\phi\left(\overline{r_1}-\overline{r}\right)\right]\right\} \quad . \tag{2.33}$$

Finally, using the definition of the autocorrelation function given by Equation (2.26), the structure function is

$$D_\phi\left(\overline{r}\right) = 2\left[\Gamma_\phi\left(0\right) - \Gamma_\phi\left(\overline{r}\right)\right] \quad . \tag{2.34}$$

For plane waves the phase structure function for Kolmolgorov turbulence is [4:34]

$$D_f\left(r\right) = 6.88\left(\frac{r}{r_0}\right)^{5/3} \quad , \tag{2.35}$$

where r is the magnitude of the radial position vector in a plane perpendicular to the direction of propagation.

2.4 Atmospheric Turbulence Modeling

One of the effects of turbulence on the propagation of light through the atmosphere is image blurring, which is due primarily to the negative effects of turbulence on phase. For a plane wave entering the Earth's atmosphere with an arbitrarily large spatial coherence, propagation over a distance L through the turbulent atmosphere results in degraded spatial coherence in the aperture plane of a collecting telescope. This degradation is measured by the transverse coherence length [5],

$$\rho_0 = \left[\frac{2.91}{2}k^2\int_0^L dz\, C_n^2\left(z\right)\right]^{-3/5} \quad , \quad \sqrt{\lambda L} < \rho < L_0 \tag{2.36}$$

$$\rho_0 = \left[\frac{3.44}{2}k^2\left(\frac{\rho}{l_0}\right)^{1/3}\int_0^L dz\, C_n^2\left(z\right)\right]^{-3/5} \quad , \quad \rho < l_0 \quad , \tag{2.37}$$

where ρ is the magnitude of the radial position vector in the plane of the aperture, ρ_0 is the separation distance beyond which two points on the wavefront in the aperture are uncorrelated, l_0 is the inner scale which corresponds to the smallest eddy size, L_0 is the outer scale which corresponds to the largest eddy size, and k is the optical wavenumber ($2\pi/\lambda$). Two key relationships should be noted based on Equations (2.36) and (2.37). First, the transverse coherence length is proportional to $\lambda^{6/5}$, and therefore image degradation due to turbulence is somewhat less in the infrared region than in the visible. Second, ρ_0 is proportional to the integrated turbulence strength. The factor $C_n^2(z)$ is the refractive index structure constant and is a measure of the strength of turbulence, but it is not truly constant and varies with time, geographic location on the earth, and altitude. Since much of the turbulence occurs at lower altitudes, major observatories around the world are built on high mountaintops to effectively reduce the integrated turbulence strength.

A much more common parameter that describes the negative effects of turbulence on spatial coherence is the atmospheric coherence length (also known as the Fried parameter) r_0, which is a translation of the transverse coherence length from the aperture plane to the focal plane. This parameter was defined in 1966 by David Fried to be the largest aperture within which the total root mean square (rms) wavefront irregularity is less than one radian (or $\lambda/2\pi$) [1]. The Modulation Transfer Function (MTF) in the focal plane [6] is

$$MTF(v) = \exp\left[-3.44\left(\lambda f v / r_0\right)^{5/3}\right] \quad , \tag{2.38}$$

where f is the focal length of the system, υ is the spatial frequency, and r_0 is the atmospheric coherence length, which is related to the transverse coherence length by $r_0 = 2.1\rho_0$. The atmospheric coherence length is thus

$$r_0 = 1.6769\left[k^2 \int_0^L dz\, C_n^2(z)\right]^{-3/5} , \quad \sqrt{\lambda L} < \rho < L_0 \qquad (2.39)$$

$$r_0 = 1.5167\left[k^2 \left(\frac{\rho}{l_0}\right)^{1/3} \int_0^L dz\, C_n^2(z)\right]^{-3/5} , \quad \rho < l_0 \quad . \qquad (2.40)$$

The effective MTF of an optical system looking through a turbulent atmosphere is simply the product of the system MTF and the MTF describing the atmosphere. Therefore turbulence has the effect of a low pass filter. The elimination of higher frequencies then results in blurring of the image.

The amplitude and intensity of the scintillated field are usually modeled as log-normal random variables. The log amplitude covariance function [5:181] is

$$C_\chi(\rho,L) = 4\pi^2 k^2 \int_0^L d\eta \int_0^\infty d\kappa\, \kappa J_0(\kappa\rho)\sin^2\left[\frac{\kappa^2(L-\eta)}{2k}\right]\Phi(\kappa,\eta) \quad , \qquad (2.41)$$

where ρ is the magnitude of the radial position vector, L is the propagation length, k is the optical wavenumber ($2\pi/\lambda$), κ is the three-dimensional spatial wavenumber, η is the variable of integration along the propagation path, and $\Phi(\kappa,\eta)$ is the power spectral density (PSD) of turbulence. The simplest PSD used to describe fluctuations in the index of refraction in the atmosphere is the Kolmogorov spectrum [4:30],

$$\Phi_n(\kappa) = 0.033 C_n^2 \kappa^{-11/3} \quad , \qquad (2.42)$$

where C_n^2 is the refractive index structure constant and κ is the three-dimensional spatial wavenumber. The spectrum of phase fluctuations is expressed in terms of r_0 and spatial frequency [4:35]:

$$\Phi_\phi\left(f_X, f_Y\right) = 0.023 r_0^{-5/3} \left(f_x^2 + f_y^2\right)^{-11/6} \quad . \tag{2.43}$$

Several other forms of the PSD of turbulence have been introduced [5:174], mostly for reasons of mathematical convenience. The following PSD [7] allows for inclusion of a finite inner scale:

$$\Phi_n(\kappa) = 0.033 C_n^2 \kappa^{-11/3} \exp\left(\frac{-\kappa^2}{\kappa_m^2}\right) \quad , \tag{2.44}$$

where $\kappa_m^2 = 5.92/l_0$ and l_0 is the inner scale. The von Karman spectrum [5:174] allows for inclusion of a finite outer scale,

$$\Phi_n(\kappa) = 0.033 C_n^2 \left(\kappa^2 + \kappa_0^2\right)^{-11/6} \quad , \tag{2.45}$$

where $\kappa_0 = 2\pi/L_0$ and L_0 is the outer scale. Finally, the modified von Karman spectrum [5:174] allows for both finite inner and outer scales,

$$\Phi_n(\kappa) = 0.033 C_n^2 \left(\kappa^2 + \kappa_0^2\right)^{-11/6} \exp\left(\frac{-\kappa^2}{\kappa_m^2}\right) \quad . \tag{2.46}$$

An expression for the modified von Karman spectra that describes phase fluctuations is

$$\Phi_\phi(f_X, f_Y) = 0.023 r_0^{-5/3} \left(f_x^2 + f_y^2 + \left(\frac{1}{L_0}\right)^2\right)^{-11/6} \exp\left(-\left(f_x^2 + f_y^2\right)^2 \left(\frac{l_0}{0.942}\right)^2\right). \tag{2.47}$$

Returning to the discussion of scintillation statistics, the log-amplitude variance is expressed in terms of the propagation length by assuming the Komologorov spectrum for

the PSD and evaluating the covariance function (Equation (2.41)) at $\rho = 0$. The required

integration is performed numerically with the following variable substitutions:

$$\alpha = \sqrt{\frac{L-\eta}{2k}}\kappa \quad ,$$
$$d\alpha = \sqrt{\frac{L-\eta}{2k}}d\kappa \quad ,$$

(2.48)

which results in the simplified covariance function

$$\sigma_\chi^2(L) = (0.132)\pi^2 (2)^{-5/6} k^{7/6} \int_0^L d\eta (L-\eta)^{5/6} C_n^2(\eta) \int_0^\infty d\alpha\, \alpha^{-8/3} \sin^2(\alpha^2) \quad . \quad (2.49)$$

The integral over α is now performed numerically, and to four decimal places it is equal

to 0.7701. Combining constants in front of the remaining integral results in a final

expression for log-amplitude variance:

$$\sigma_\chi^2(L) = (0.5631)k^{7/6} \int_0^L d\eta (L-\eta)^{5/6} C_n^2(\eta) \quad . \quad (2.50)$$

Equation (2.50) describes the variance of the log of the amplitude in a plane wave after

propagating a distance L. For the log-amplitude variance of an optical field at the earth's

surface due, for example, to an observed star, the point $\eta = 0$ corresponds to the location

at which the plane wave enters the earth's atmosphere and the point $\eta = L$ is determined

by the thickness of the atmosphere traversed. This equation can also be expressed so that

the zero-point corresponds to the location of a ground-based observer. In this case the

integration is carried out from the ground up to a desired altitude:

$$\sigma_\chi^2(L) = (0.5631)k^{7/6} \int_0^L d\beta (\beta)^{5/6} C_n^2(\beta) \quad . \quad (2.51)$$

The important physical interpretation of the expressions for log-amplitude variance is that

for a given point along the integration path through the atmosphere, the strength of

turbulence is weighted by a factor proportional to the remaining distance to the observation point on the ground. For astronomical imaging at near zenith, mild turbulence is often modeled by a single phase screen at the telescope pupil. For extended turbulence that results in scintillation in addition to a wrinkled phase profile, the phase is distorted at some distance from the pupil (or target), which means that the individual tilted portions of wavefront eventually interfere with each other. The resulting destructive and constructive interference is termed scintillation.

2.5 Sampling Theory

There are two critical relationships that involve sampling and the Discrete Fourier Transform (DFT). First, for N samples of a signal in the spatial (or temporal) domain separated by Δx, the frequency domain signal obtained by taking the DFT is also repeated every N samples, or $1/\Delta x$ in terms of frequency. Conversely, N samples in the frequency domain separated by $\Delta \xi$ correspond to a spatial domain signal which repeats every N samples, or $1/\Delta \xi$ in terms of space (or time) units. These relationships are illustrated in Figure 2.1.
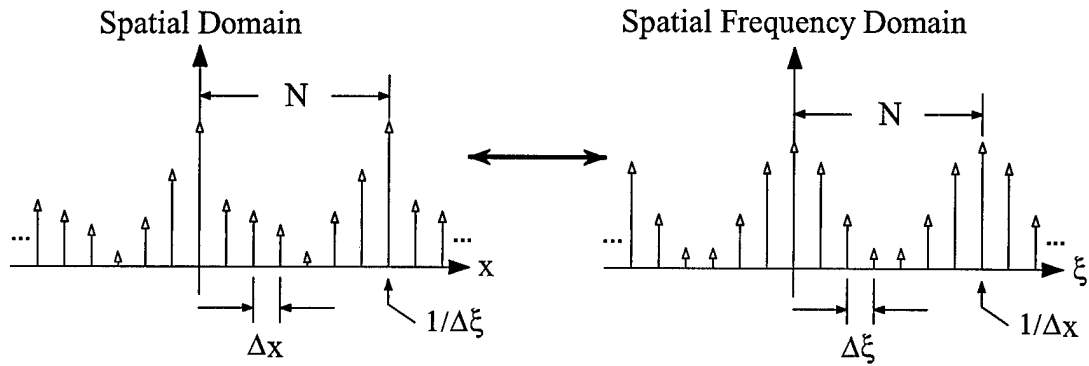
Figure 2.3. Sampling and the Discrete Fourier Transform

The other critical relationship pair relates the spacing in one domain to the sampling parameters in the other:

$$\Delta\xi = \frac{1}{N\Delta x} \quad , \tag{2.52}$$

which is also

$$\Delta x = \frac{1}{N\Delta\xi} \quad , \tag{2.53}$$

The matrices used in the propagation algorithms are setup as in Figure 2.4. Here values inside the matrix indicate pixel distance from the origin. The Fresnel approximation to the free space propagation transfer function (Equation (2.20)) is used for all simulations. Note that to avoid aliasing of the propagator, for a generic phasor the separation between samples of the phase angle must be less than or equal to π. The phase angle of the Fresnel propagator is a quadratic function of spatial frequency, and thus the largest difference between adjacent pixels occurs at the four corners of the matrix.

Index 1 2 3 . . . $\frac{N+2}{2}$ . . . N

	1	2	3				$\frac{N+2}{2}$				N
1											
2		$\frac{N-2}{\sqrt{2}}$					$\frac{N-2}{2}$				$\frac{N-2}{\sqrt{2}}$
3			.				.			.	
.				.			.			.	
.					.		.		.		
.						$\sqrt{2}$	1	$\sqrt{2}$			
$\frac{N+2}{2}$		$\frac{N-2}{2}$	.	.	.	1	0	1	.	.	.	$\frac{N-2}{2}$
.						$\sqrt{2}$	1	$\sqrt{2}$			
.					.		.		.		
.				.			.			.	
.			.							.	
N		$\frac{N-2}{\sqrt{2}}$					$\frac{N-2}{2}$				$\frac{N-2}{\sqrt{2}}$

Figure 2.4. Propagation Matrix Setup

Taking the lower right corner as an example, the difference between pixel (N, N) and pixel (N-1, N-1) must satisfy the previously stated requirement. This outermost diagonal distance clearly contains the greatest adjacent change. The squared spatial frequency in any one of the four outermost corners is, in general,

$$\left[\left(\frac{N-2}{2}\right)^2 + \left(\frac{N-2}{2}\right)^2\right](\Delta\xi)^2 \quad . \tag{2.54}$$

The squared spatial frequency in the immediately adjacent pixel along the diagonal is

$$\left[\left(\frac{N-2}{2}-1\right)^2 + \left(\frac{N-2}{2}-1\right)^2\right](\Delta\xi)^2 \quad . \tag{2.55}$$

Taking the difference between Equations (2.54) and (2.55), the maximum difference in squared spatial frequency is now

$$\Delta \kappa^2_{max} = 2\left(\Delta \xi\right)^2 \left[\left(\frac{N-2}{2}\right)^2 - \left(\frac{N-4}{2}\right)^2\right] \quad . \tag{2.56}$$

The condition imposed on the complex exponential describing Fresnel propagation is

$$\Delta \phi_{max} = \pi \lambda z 2\left(\Delta \xi\right)^2 \left[\left(\frac{N-2}{2}\right)^2 + \left(\frac{N-4}{2}\right)^2\right] \leq \pi \quad . \tag{2.57}$$

Using equation (2.52), the aliasing constraint is

$$\frac{2\lambda z\left(N-3\right)}{\left(N\Delta x\right)^2} \leq 1 \quad . \tag{2.58}$$

If N is much larger than 3 then the (N-3) term in the numerator can be replaced by N, which allows Equation (2.58) to be expressed in a simpler form:

$$N \geq \frac{2\lambda z}{\left(\Delta x\right)^2} \quad . \tag{2.59}$$

Here N is normally at least 128 for propagation simulations such as those reported here, and thus, the above assumption is valid.

Note that Equation (2.59) can be interpreted as a requirement that N be greater than the number of pixels that would fit into the main lobe of the Fraunhofer diffraction pattern resulting from a square aperture of dimensions equal to the pixel spacing Δx. Along one dimension in the plane containing such a diffraction image, the width of the central intensity lobe is

$$x = \frac{\lambda R}{a} \quad , \tag{2.60}$$

where the x and y axes are in the plane of the diffraction pattern located a distance z from the aperture, R is the straight-line distance from the center of the aperture (at $z = 0$) to the point in the diffraction pattern, and a is the dimension of the square aperture. For small angles between the vector defined by R and the optic axis, Equation (2.60) clearly simplifies to

$$x = \frac{\lambda z}{a} \quad , \tag{2.61}$$

which is easily recognized as the distance from the origin to the first intensity null in the diffraction pattern from a narrow slit of width a. Comparing Equations (2.61) and (2.59), the aliasing constraint is interpreted as a requirement that the number of pixels along one dimension of the propagator matrix must be at least equal to the number of equally sized pixels that would fit into the diffraction pattern created by a single pixel located at a distance z from the propagator.

3. Phase Screen Generation

3.1 Creation of Test Fields

The atmosphere is often modeled by a set of discrete turbulence layers [8:66-67]. This layered approach is used to create scintillated test fields, which are then used to evaluate the performance of the two deformable mirror phase conjugating system. The log-amplitude variance is employed to drive the other parameters of the layered model. A discrete version of Equation (2.51) is needed to create the model:

$$\sigma_\chi^2(L) = 0.5631 k^{7/6} \sum_{i=1}^{M} z_i^{5/6} C_{n_i}^2 \Delta z_i \quad , \tag{3.1}$$

where M is the number of layers in the model, L is the thickness of the atmosphere being traversed, z_i and Δz_i are the height and thickness of a specific layer, respectively, and $C_{n_i}^2$ describes the strength of turbulence in a given layer. To further simplify this expression the strength of turbulence in each layer is expressed as a fraction of the total integrated turbulence,

$$W_i I_C = C_{n_i}^2 \Delta z_i \quad , \tag{3.2}$$

where I_C is the total integrated value of C_n^2 and W_i is a weighting factor corresponding to the relative strength of turbulence in a given layer such that $\sum_{i=1}^{M} W_i = 1$. Equation (3.2) can now be employed to rewrite Equation (3.1) as an expression for I_C as a function of σ_χ^2:

$$I_c\left(\sigma_\chi^2\right) = \frac{\sigma_\chi^2}{(0.5631)k^{7/6}\sum_{i=1}^{M}W_i z_i^{5/6}} \quad . \tag{3.3}$$

The same approach may be used to modify Equation (2.39):

$$r_0 = 1.6769\left[k^2 I_c \sum_{i=1}^{M}W_i\right]^{-3/5}, \quad \sqrt{\lambda L} < \rho < L_0 \quad . \tag{3.4}$$

Using the fact that the weight vector W_i sums to one and substituting Equation (3.3) for the total integrated turbulence, the atmospheric coherence diameter may be expressed as a function of log-amplitude variance:

$$r_0\left(\sigma_\chi^2\right) = \frac{1.1881}{\sqrt{k}}\left[\frac{1}{\sigma_\chi^2}\sum_{i=1}^{M}W_i z_i^{5/6}\right]^{3/5}, \quad \sqrt{\lambda L} < \rho < L_0 \quad . \tag{3.5}$$

For the turbulence strength profile given below, values of r_0 and C_n^2 are obtained based on σ_χ^2 values of 0.1, 0.2 ... 1.0. Once these values are produced a series of scintillated test fields are created using an outer scale value of $L_0 = \infty$. The phase screens through which a wavefront is propagated to created scintillated fields are created using the well-known FFT approach [9] and the Kolmolgorov spectrum. The Kolmolgorov PSD is obtained from the von Karman PSD given by Equation (2.47) by letting the outer scale (L_0) go to infinity and the inner scale (l_0) go to zero,

$$\Phi_\phi(\xi,\eta) = 0.023 r_0^{-5/3}\left(\xi^2 + \eta^2\right)^{-11/6} \quad , \tag{3.6}$$

where ξ and η are the spatial frequency variables along x and y, respectively. The atmospheric phase screens are generated by filtering complex white Gaussian noise with the square root of the Kolmorgorov power spectrum, which serves to force the power

3-2

spectrum (and autocorrelation) to match that of the Komolgorov spectrum. The phase

screens are generated numerically with the aid of the DFT,

$$\phi\left(n\Delta x, m\Delta x\right) = \mathrm{Re}\left\{DFT\left\{\sqrt{P(p,q)}\left[a(p,q)+ib(p,q)\right]\right\}\right\}$$
$$\text{or} \tag{3.7}$$
$$\phi\left(n\Delta x, m\Delta x\right) = \mathrm{Im}\left\{DFT\left\{\sqrt{P(p,q)}\left[a(p,q)+ib(p,q)\right]\right\}\right\}$$

where Δx is the phase screen sample spacing, $P(p,q)$ is the power associated with the

spatial frequency $\xi = p\Delta\xi$ and $\eta = q\Delta\xi$, $\Delta\xi$ is the sample spacing in Fourier (frequency)

space (see Equation (2.52)), and a and b are pseudo random numbers generated from a

Gaussian distribution with zero-mean and unit-variance. The power associated with each

sample in Fourier space is

$$P(p,q) = \Phi_\phi\left(p\Delta\xi, m\Delta\xi\right)\Delta\xi^2 \tag{3.8}$$

Using Equations (3.6), (3.8), and (2.52), the phase screen is now described by

$$\phi\left(n\Delta x, m\Delta x\right) = 0.1517\left(\frac{L}{r_0}\right)^{5/6}\mathrm{Re}\left\{DFT\left\{\left(\xi^2+\eta^2\right)^{-11/12}\left[a(p,q)+ib(p,q)\right]\right\}\right\}$$
$$\text{or} \tag{3.9}$$
$$\phi\left(n\Delta x, m\Delta x\right) = 0.1517\left(\frac{L}{r_0}\right)^{5/6}\mathrm{Im}\left\{DFT\left\{\left(\xi^2+\eta^2\right)^{-11/12}\left[a(p,q)+ib(p,q)\right]\right\}\right\} \quad .$$

3.1.1 NOP Test Scenario

In support of the ABL program, test data have been collected recently at North

Oscura Peak (NOP) in New Mexico. A "beacon" laser was fired from an aircraft to a site

atop NOP. Another laser, modified using adaptive optics driven by the sensed beacon

field, then was fired back toward the aircraft. The data collected from the NOP

experiments may represent the actual engagement conditions anticipated for ABL. Three

different aircraft-NOP radial distances were used for collecting data: 35, 42, and 54 km. For the purpose of the NOP simulations reported here, a propagation distance of 50 km is used. The turbulence experienced along that path is modeled using ten phase screens.

For the simulation scenario, the screen furthest from NOP is placed at a horizontal distance of 50 km, and the remaining screens are spaced evenly between the peak (0 km) and the final screen. The strength of turbulence is assumed to be equal at each of the screens, resulting in the following weight vector:

$$W_{\mathrm{NOP}} = \begin{bmatrix} \frac{1}{10} & \frac{1}{10} & \frac{1}{10} & \frac{1}{10} & \frac{1}{10} & \frac{1}{10} & \frac{1}{10} & \frac{1}{10} & \frac{1}{10} & \frac{1}{10} \end{bmatrix} . \tag{3.10}$$

Also, an optical wavelength of 1 μm is used for all simulations, which is representative of the ABL system. Table 1 summarizes the NOP test scenario simulation parameters.

Table 1. NOP Test Scenario Simulation Parameters

σ_χ^2	$C_n^2 \ (\times 10^{-12}\,\mathrm{m}^{-2/3})$	r_0 (cm)	$2\lambda L/\Delta x^2$ (pixels)
0.1	0.42488	30.884	16.77
0.2	0.84977	20.376	38.54
0.3	1.27465	15.976	62.69
0.4	1.69953	13.443	88.54
0.5	2.12442	11.758	115.72
0.6	2.54930	10.540	144.03
0.7	2.97418	9.609	173.29
0.8	3.39907	8.869	203.41
0.9	3.82395	8.264	234.29
1.0	4.24883	7.758	265.86

3.2 Comparison of Simulated Phase Screen Statistics to Theory

Several statistics of the FFT-generated random phase screens are measured and compared to theory in the following section. For all of the following statistical analyses, a value of 10 cm is used for the Fried parameter, and the sampling interval is set to $\frac{1}{4}r_0$ (2.5 cm). A sample screen is plotted as a three-dimensional surface in Figure 3.1 and as a bitmap in Figure 3.2.
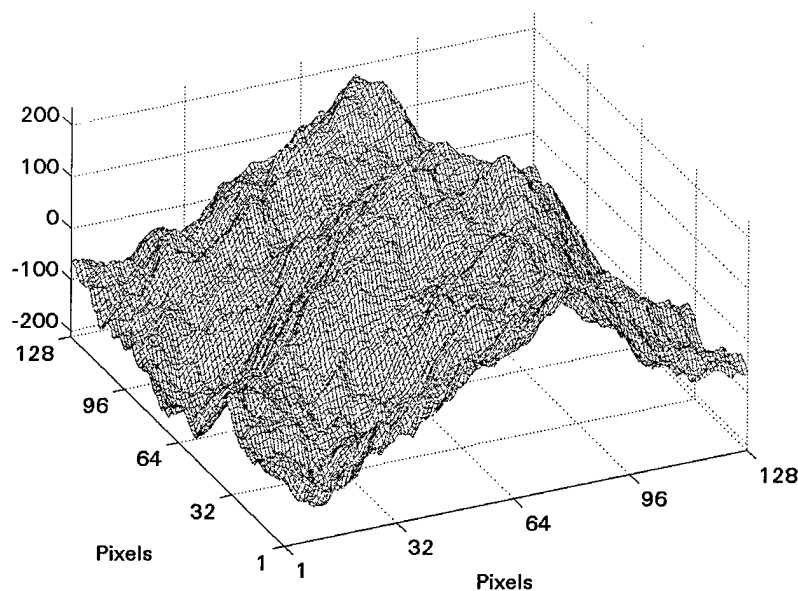

Figure 3.1. Surface Plot of One Realization of a Random Phase Screen (Using Kolmolgorov Spectrum with $\Delta x = 10$ cm and $r_0 = 2.5$ cm)
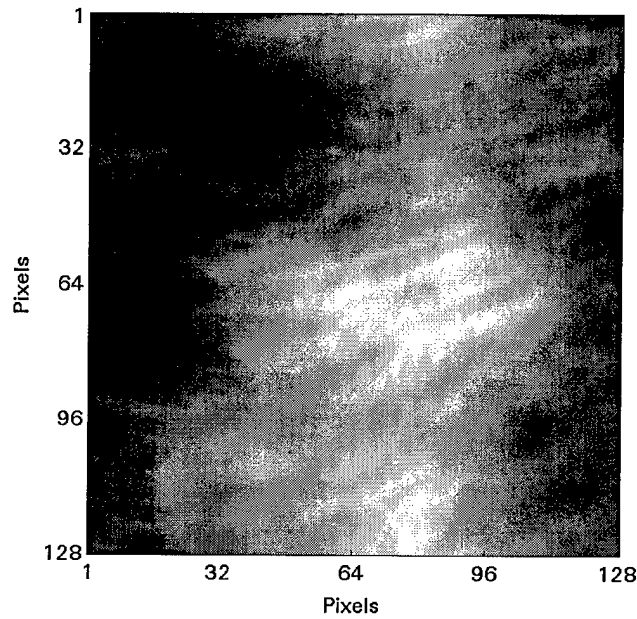
Figure 3.2. Bit-map of One Realization of a Random Phase Screen (Using Kolmolgorov Spectrum with $\Delta x = 10$ cm and $r_0 = 2.5$ cm)

3.2.1 Phase Variance (Tilt Removed) vs. Aperture Size

In order to verify correct operation of the FFT-based phase screen generator, several realizations were created to measure statistical properties. The mean phase variance versus square aperture width (normalized to r_0) is plotted in Figure 3.3 for 100 phase screen realizations generated using the Kolmolgorov spectrum. The mean phase variance versus circular aperture diameter (normalized to r_0) is also plotted in Figure 3.4 for 100 phase screen realizations generated using the Kolmolgorov spectrum. In both cases the variance is calculated for a set of increasing aperture dimensions by extracting the pixels captured by a given aperture (mask), removing piston and Zernike tilt, and

calculating the variance of their values. One hundred vectors containing variance versus aperture size are thus created and averaged.
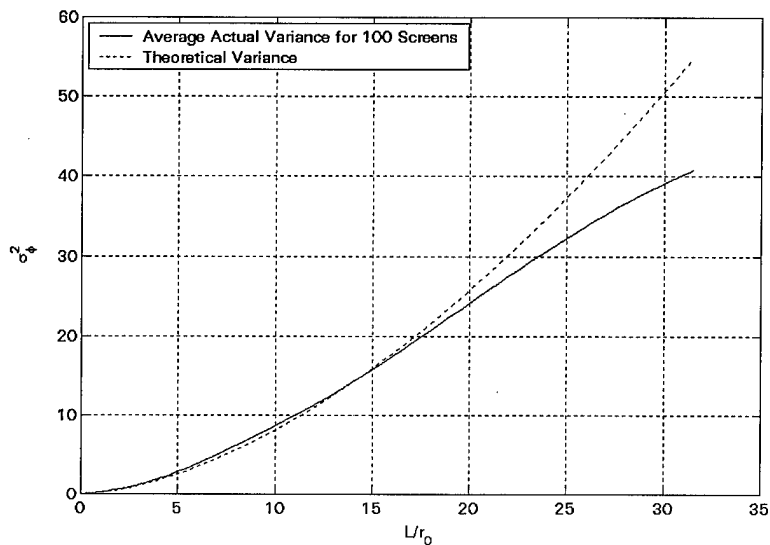

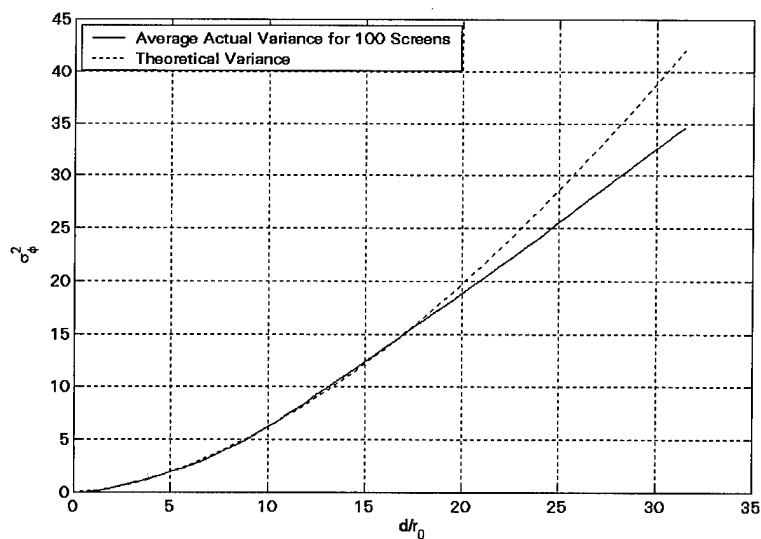**Figure 3.3. Phase Variance vs. L/r_0 for a Square Aperture**

Figure 3.4. Phase Variance vs. d/r_0 for a Circular Aperture

3.2.2 Autocorrelation

The mean autocorrelation of the phase is plotted in Figure 3.5 for 100 phase

screen realizations generated using the Kolmolgorov spectrum. The autocorrelation of a

single realization tends to deviate significantly from the smooth surface shown in Figure

3.5 near the outer portions of the discretely sampled surface due to the fact that fewer

data points are available to average as the magnitude of the separation vector r

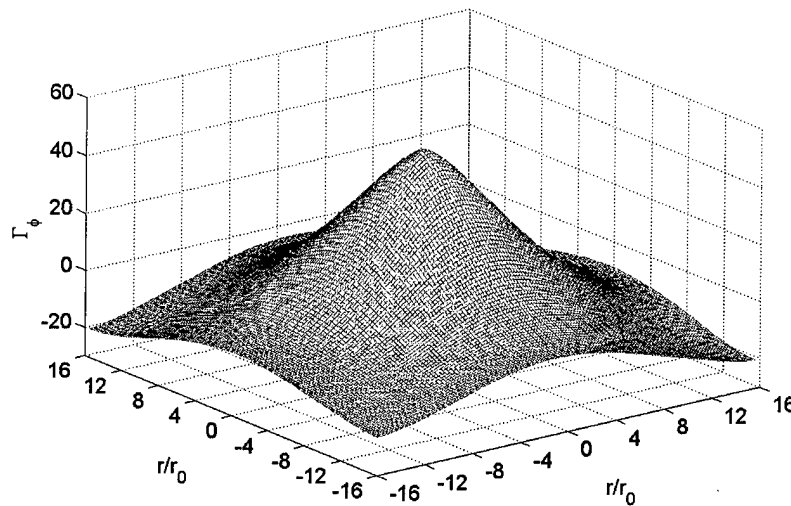approaches one-half the diagonal distance across the matrix.

Figure 3.5. Phase Autocorrelation Function

3.2.3 Phase Structure Function vs. d/r_0

The mean phase structure function is plotted in Figure 3.6 as a three-dimensional

surface (using Equation (2.34)) for 100 phase screen realizations generated using the

Kolmolgorov spectrum. The averaged cross section of this surface is displayed in Figure

3-8

3.7. One of the documented reasons for the disparity between the theoretical and actual

phase structure functions is the loss of low frequency content due to sampling of the

Kolmolgorov spectrum [10]. The lowest frequency in the sampled spectrum is $1/x$, where

x the physical width represented by an array of samples. This negative effect can be

offset to some degree by increasing the number of samples (for a constant spacing), but

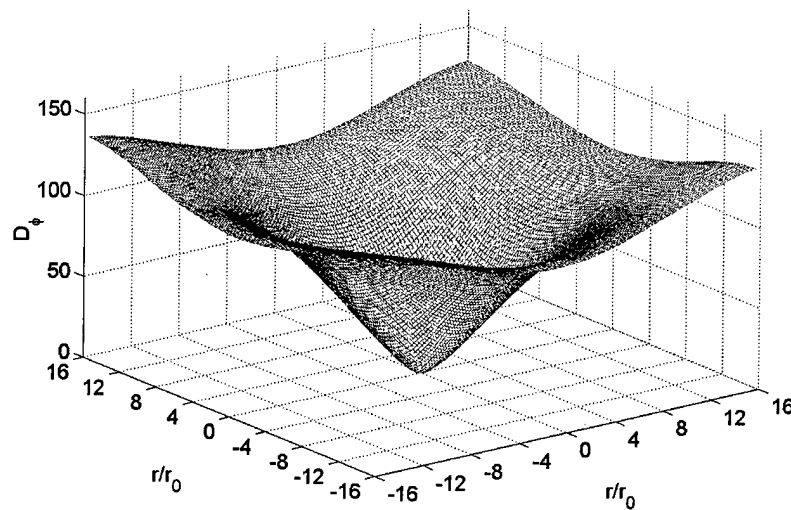this remedy obviously imposes greater computational requirements.

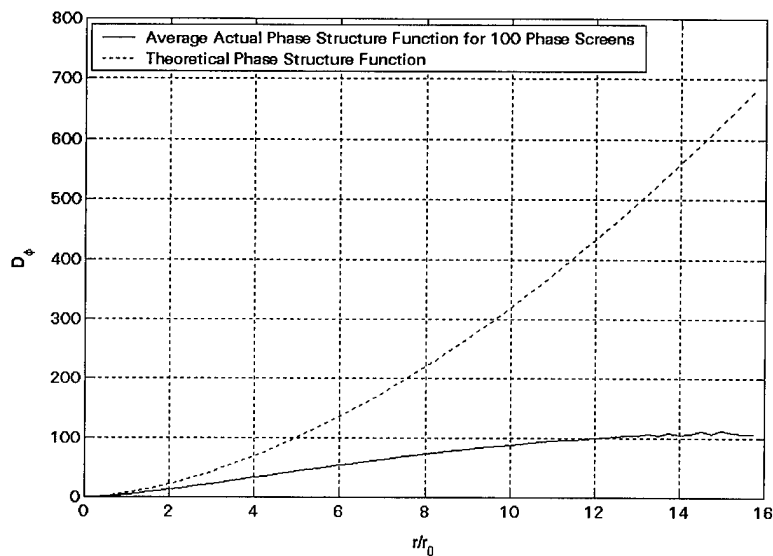**Figure 3.6. Mean Phase Structure Function (Surface Plot)**

Figure 3.7. Mean Cross-Section of the Phase Structure Function

3.3 Comparison of Simulated Scintillated Amplitude Field Statistics to Theory

3.3.1 Log-Amplitude Variance

The mean log-amplitude variance (Rytov parameter) values for an ensemble of 32 independent realizations are displayed in Figure 3.8. The saturation of the actual Rytov parameter for the simulated fields agrees with empirical data [5:186-7].
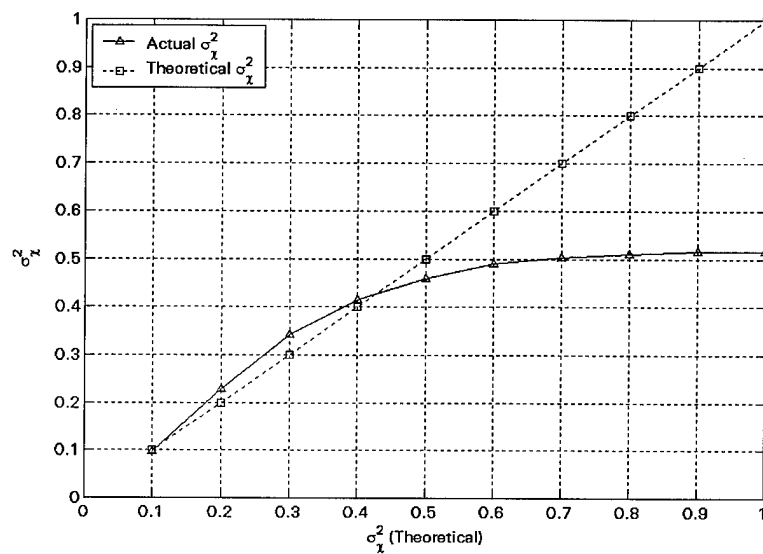
Figure 3.8. Log-Amplitude Variance for Simulated Beacon Fields

4. Sequential Generalized Projection Algorithm (SGPA)

4.1 Physics-Based Algorithm Development

Following the earlier discussion on wavefront propagation, the operator $T_z [\cdot]$ indicates Fresnel propagation (given by Equation (2.20)) of a field over a distance z, and $T_z^* [\cdot]$ indicates propagation in the opposite direction. The new field at the plane defined by z is then

$$U_z (\vec{r}') = T_z \left[U_0 (\vec{r}) \right] = \mathcal{F}^{-1} \left\{ \mathcal{F} \left[U_0 (\vec{r}) \right] e^{i\pi\lambda z \vec{\kappa}^2} \right\} \quad , \tag{4.1}$$

where $\mathcal{F}$ denotes the two-dimensional Fourier transform, z is the distance of propagation between the two deformable mirrors, $\vec{r}$ is the position vector in the plane at $z = 0$, and $\vec{r}'$ is the position vector in the plane at $z = z$. The on-axis far-field intensity of the laser beam is proportional to the degree to which optical phase conjugation is achieved. The outgoing field after reflection from DM2 is

$$U_z (\vec{r}') = U_I (\vec{r}') e^{i\phi_2 (\vec{r}')} \quad . \tag{4.2}$$

The outgoing field after reflection from DM1 is

$$U_0 (\vec{r}) = T_z \left[U_z (\vec{r}') \right] e^{i\phi_1 (\vec{r})} = T_z \left[U_I (\vec{r}') e^{i\phi_2 (\vec{r}')} \right] e^{i\phi_1 (\vec{r})} \quad . \tag{4.3}$$

Again, the far-field intensity of the beam is proportional to the degree to which phase conjugation is achieved, i.e.,

$$I \propto \left| \int dr\, U_b (\vec{r}) U_0 (\vec{r}) \right|^2 \quad . \tag{4.4}$$

Substituting Equation (4.3) into Equation (4.4) and applying a scale factor so that I ranges from 0 to 1 yields

$$I = \frac{\left|\int dr\, U_b(\bar{r}) e^{i\phi_1(\bar{r})} T_z\left[U_l(\bar{r}') e^{i\phi_2(\bar{r}')}\right]\right|^2}{\left|\int dr\, U_b(\bar{r}) U_b^*(\bar{r})\right| \left|\int d\bar{r}'\, U_l(\bar{r}') U_l^*(\bar{r}')\right|} \qquad . \tag{4.5}$$

Now the goal is to determine phase commands that maximize I when applied to DM1 and DM2. A local maximum is located by iteratively solving for the values of ϕ_1 and ϕ_2 that maximize I (with all other values fixed). Clearly, the numerator of Equation (4.5) is maximized if the phase of the laser wavefront is the conjugate of the phase of the incoming beacon field. This condition requires the integration of a purely real number. With all other values fixed, the ideal value for ϕ_1 is

$$\phi_1 \Big|_{I\max} = \arg\left\{ U_b^*(\bar{r}) T_z\left[U_l(\bar{r}') e^{i\phi_2(\bar{r}')}\right]^* \right\} \qquad . \tag{4.6}$$

An expression for ϕ_2 is found with the aid of a generalized form of Rayleigh's theorem (i.e., the energy theorem, Parseval's theorem, or Plancherel's theorem),

$$\int_{-\infty}^{\infty} d\alpha\, f(\alpha) g^*(\alpha) = \int_{-\infty}^{\infty} d\beta\, F(\beta) G^*(\beta) \qquad , \tag{4.7}$$

plus a basic property of Fourier transforms:

$$f^*(\pm x) \Leftrightarrow F^*(\mp \xi) \qquad . \tag{4.8}$$

Applying Equation (4.7) twice and invoking Equation (4.8) to simplify results, the formula for I is

$$I = \frac{\left|\int d\bar{r}'\, U_l(\bar{r}') e^{i\phi_2(\bar{r}')} T_z\left[U_b(\bar{r}) e^{i\phi_1(\bar{r})}\right]\right|^2}{\left|\int dr\, U_b(\bar{r}) U_b^*(\bar{r})\right| \left|\int d\bar{r}'\, U_l(\bar{r}') U_l^*(\bar{r}')\right|} \qquad . \tag{4.9}$$

A relationship for manipulating these expressions is formulated using Equation (4.8) and the fact that for energy projection applications the inversion of coordinates is inconsequential. Thus

$$\left\{ T_z[U] \right\}^* = T_z^* \left[U^* \right] \tag{4.10}$$

or

$$\left\{ T_z\left[U^*\right] \right\}^* = T_z^*[U] \quad . \tag{4.11}$$

From Equation (4.9) the optimal value of ϕ_2 with all other quantities fixed is

$$\phi_2 \bigg|_{I\,\text{max}} = \arg\left\{ U_i^*(\vec{r}\,') T_z\left[U_b(\vec{r})\, e^{i\phi_1(\vec{r})} \right]^* \right\} \quad . \tag{4.12}$$

The above algorithm derivation was originally developed by Ellerbroek [11, 12].

4.2 Branch Points and Least Squares Reconstruction

Wavefront sensors normally provide data that indirectly describe the wavefront phase. In the case of the Shack-Hartmann sensor, quantities proportional to wavefront slopes are obtained. The slopes are related to the phases by

$$\mathbf{g} = \mathbf{G}\mathbf{\Phi} \quad , \tag{4.13}$$

where $\mathbf{G}$ is a matrix describing the geometrical configuration of wavefront sensor positions and phase determination positions [4:258]. In a closed-loop implementation, where $\mathbf{G}$ includes the effect of a deformable mirror, $\mathbf{G}$ is often referred to as the *influence* or *poke* matrix. The least squares estimate for the phase is

$$\hat{\mathbf{\Phi}} = \left(\mathbf{G}^T \mathbf{G} \right)^{-1} \mathbf{G}\mathbf{g} \quad . \tag{4.14}$$

The propagation of a coherent monochromatic optical field through a turbulent atmosphere (where the field is subject to spatially varying phase perturbations) results in constructive and destructive interference in the amplitude (or intensity) of the field. Locations in the field where the amplitude goes to zero indicate the presence of a branch

4-3

point. In practice, branch points in an optical field are located by summing the principal value gradients around the smallest possible closed contour, where the principal value operator $PV[\cdot]$ simply produces an equivalent phase in the range $-\pi$ to π. If a branch point is enclosed, then the contour integral of principal value phase gradients equals $\pm 2\pi$. Likewise, if a branch point is not enclosed then the contour integral equals zero. The least squares estimator for the phase does not correctly reconstruct the phase if branch points are present because of the underlying assumption, made by the least squares estimator, that the measured slopes are indicative of the gradient of a scalar phase function. Actually, the function describing the gradient of the perturbed phase must be treated as the sum of the gradient of a scalar potential and the curl of a vector potential, i.e.,

$$\mathbf{g}(r) = \nabla s(r) + \nabla \times \mathbf{H}(r) \quad , \tag{4.15}$$

where r is a position vector of x and y components, s(r) is a scalar potential, and H(r) is a vector potential. Since g(r) only has components in the x and y directions, H(r) clearly has non-zero components only in the z direction.

In going from a discrete space to a continuous formulation, the $\mathbf{G}$ matrix above can be equated to the gradient operator, $\mathbf{G}^{\mathrm{T}}$ can be equated to the divergence operator, and $\mathbf{G}^{\mathrm{T}}\mathbf{G}$ can be equated to the laplacian operator. This formulation allows additional insight into the operation of the least squares reconstructor. Equation (4.14) describing the least squares estimate is recast in a continuous space formulation as

$$\nabla^2 \hat{\mathbf{\Phi}}(r) = \nabla \cdot \left[\nabla s(r) + \nabla \times \mathbf{H}(r) \right] \quad . \tag{4.16}$$

Recalling the vector identity stating that the divergence of the curl of a vector is equal to zero, Equation (4.16) becomes

$$\nabla^2 \hat{\Phi}(r) = \nabla \cdot \left[\nabla s(r) \right] \quad, \tag{4.17}$$

which indicates that the least squares estimate for the phase has completely ignored the contribution from the vector potential. The actual phase can now be defined as

$$\phi(r) = \hat{\phi}(r) + \phi_{hid}(r) \quad, \tag{4.18}$$

where $\phi_{hid}(r)$ is the "hidden" phase unaccounted for in the least squares reconstruction [13].

The components of Equation (4.18) are plotted in Figures Figure 4.1 through Figure 4.6 for the phase of one realization of a scintillated test field with a theoretical log-amplitude variance of 0.3. Figure 4.1 and Figure 4.2 show a bitmap and a three-dimensional surface of the wrapped phase, respectively. Figure 4.3 and Figure 4.4 show the least squares reconstruction of the phase; this continuous surface is a form that is realizable by a continuous facesheet deformable mirror. The hidden phase (containing the branch points) is displayed in Figures Figure 4.5 and Figure 4.6 and contains abrupt changes that are difficult for a continuous facesheet deformable mirror to realize in practice.
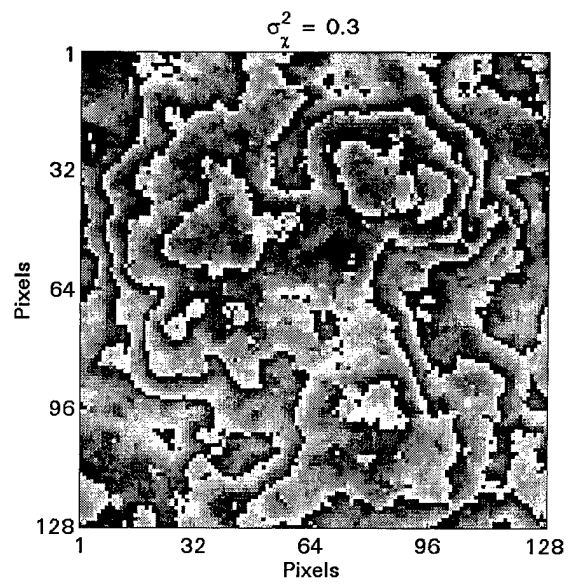
Figure 4.1. Wrapped Phase Map for One Scintillated Test Field with a Log-Amplitude Variance of 0.3 (Bitmap)
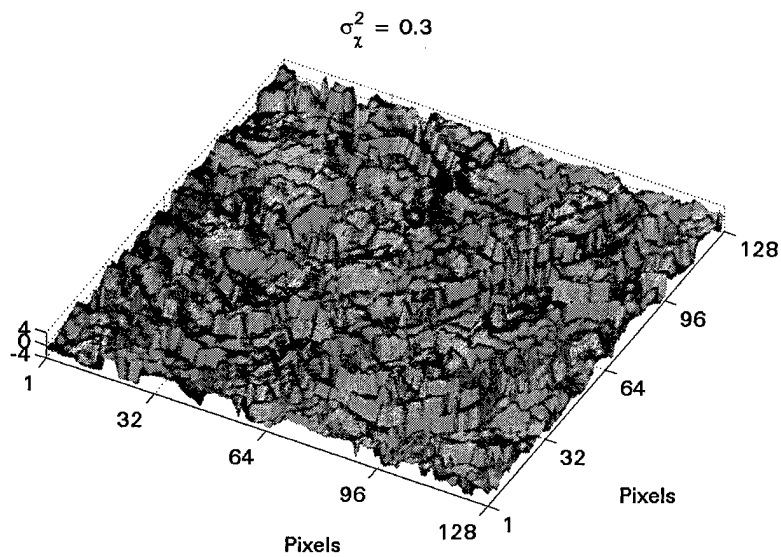
Figure 4.2. Wrapped Phase Map for One Scintillated Test Field with a Log-Amplitude Variance of 0.3 (Surface)
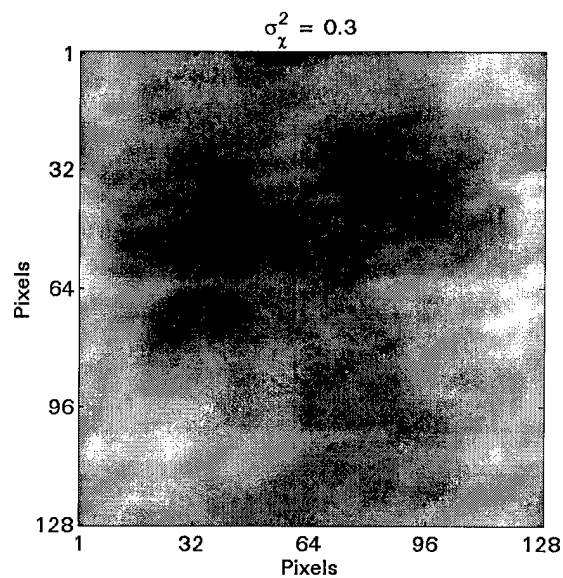
Figure 4.3. Least Squares Reconstruction of a Wrapped Phase Map for One Scintillated Test Field with a Log-Amplitude Variance of 0.3 (Bitmap)
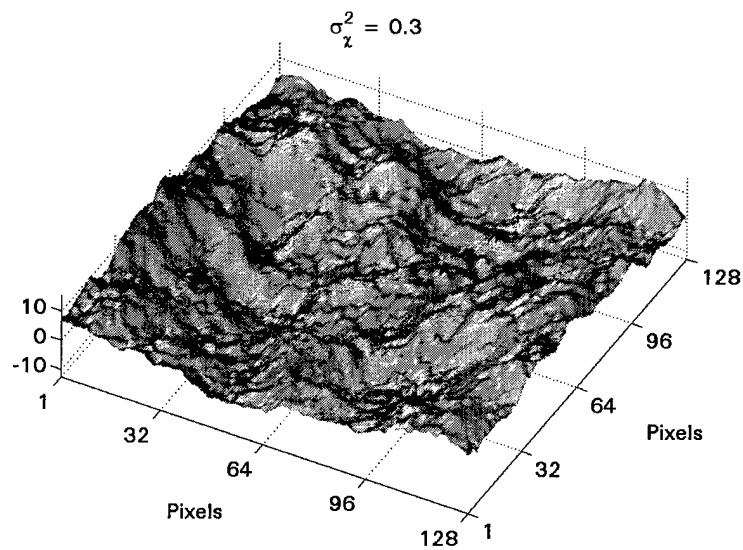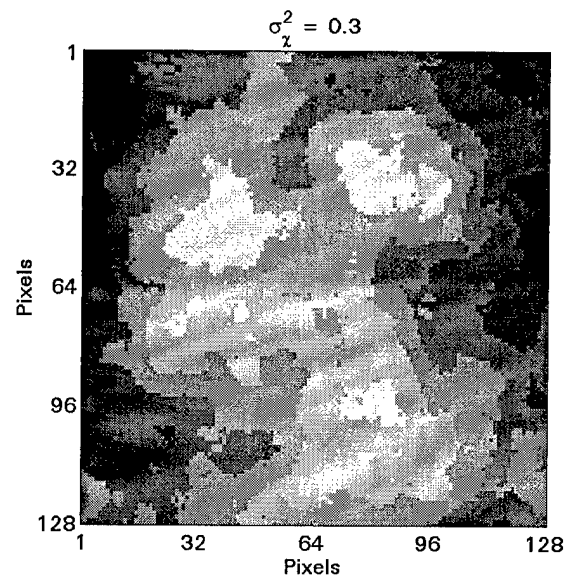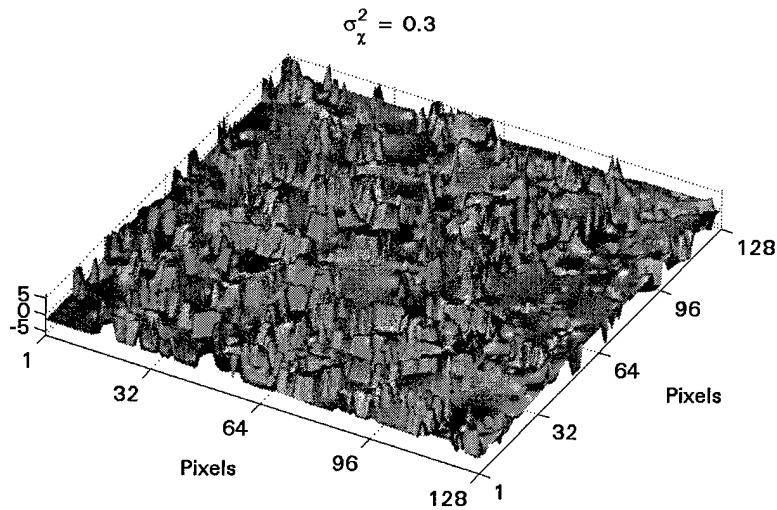

Figure 4.4. Least Squares Reconstruction of a Wrapped Phase Map for One Scintillated Test Field with a Log-Amplitude Variance of 0.3 (Surface)

Figure 4.5. Hidden Phase Contribution of a Wrapped Phase Map for One Scintillated Test Field with a Log-Amplitude Variance of 0.3 (Bitmap)

Figure 4.6. Hidden Phase Contribution of a Wrapped Phase Map for One Scintillated Test Field with a Log-Amplitude Variance of 0.3 (Surface)

5. Results and Analysis

Scintillated beacon fields are created using FFT-based phase screen generation and Fresnel propagation to evaluate the performance of the SGPA algorithm. All simulations are accomplished using MATLAB version 5.3. The test set is based on an ABL-type scenario and North Oscura Peak (NOP) testing in support of ABL. A total of 32 fields (and the corresponding 10 screen atmospheric models) are created for Rytov parameter values of 0.1, 0.2,..., 1.0. The outer scale (L_0) is set to ∞ for all simulations. Intensity plots of one scintillated field realization for each Rytov parameter value are provided as a visual reference in Appendix A.

For comparison the phase only Strehl, least squares phase only Strehl, least squares 2-DM Strehl, and uncompensated Strehl are plotted in addition to the 2-DM Strehl versus the Rytov parameter. Furthermore, all five Strehls are computed both inside the telescope and beyond the telescope at the "top" of the atmospheric model for the Strehl versus Rytov parameter analysis. The "outer" Strehl is computed in four different versions corresponding to increasing levels of realism.

5.1 Strehl Ratio vs. the Gaussian Laser Beam Profile

As stated previously, the input aperture of the telescope is set to 31 pixels in radius for all simulations. The optimal shape of the Gaussian amplitude profile is analyzed by plotting Strehl ratio versus location of the 1/e point in the Gaussian amplitude field. It is assumed that the appropriate optics would be available in an actual hardware implementation such that the location and size of the beam waist could be

manipulated; therefore, the shape of the beam is optimized in the plane of the input

aperture. This method eliminates any dependence of the optimized value on the

conjugate range of DM2. Also, to further limit the influence of other parameters on the

results of this simulation, the total energy in the Gaussian beam is kept constant for all

beam shapes. This is easily accomplished by examining the standard equation describing

the amplitude of a Gaussian beam [14:70]:

$$\left|\frac{E(x,y,z)}{E_0}\right| = \frac{w_0}{w}\exp\left[-\left(\frac{r}{w}\right)^2\right] \quad ,\qquad (5.1)$$

where w_0 is the beam waist and w is the radial location of the 1/ e point in the amplitude

field (which is a function of distance z in an actual Gaussian beam). For the purpose of

the modeling at hand, a "default" beam waist (w_0) is arbitrarily chosen to be 31 pixels in

radius. Actually, the beam waist is the closest the 1/e point ever gets to the axis of

propagation, but for the simulations the 1/e point was allowed to range from 5 to 60

pixels, thereby covering nearly all of the 128 x 128 beacon field. Setting the waist to a

constant simply maintains a constant energy in the beam. The appropriate scaling of the

peak amplitude by Equation (5.1) accomplishes this task mathematically, maintaining a

constant value of the integrated intensity.

Note from Figures 5.1 to 5.3 that the variation of Strehl with location of the 1/e

point decreases with increasing Rytov parameter. From this perspective stronger

turbulence is advantageous because system performance is less dependent on the degree

and accuracy to which the Gaussian beam profile can be controlled. The peak value of

the curves tends to increase with strength of turbulence to some extent, which doesn't

correctly describe the actual performance of the system as scintillation increases. The

next step toward a more realistic analysis would be to penalize the Strehl for laser energy

under the Gaussian curve not accounted for by the finite propagation matrix, which

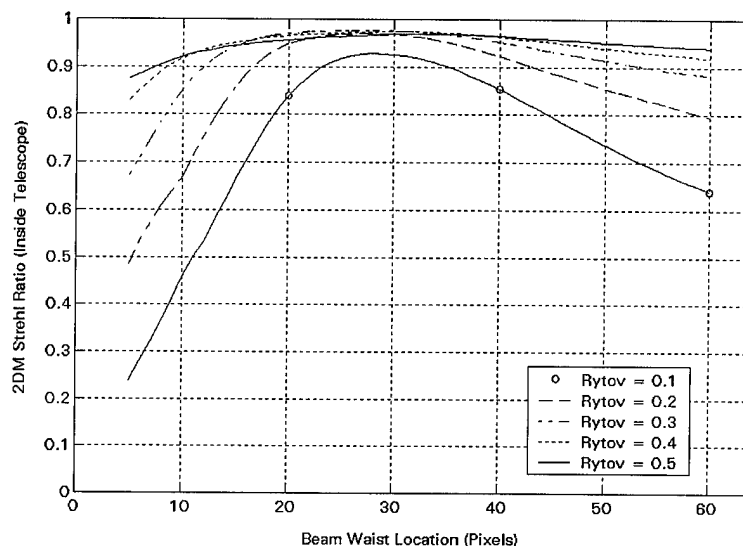becomes significant as the waist approaches the edge of the matrix.

Figure 5.1. 2-DM Strehl Ratio (Inside Telescope) vs. Gaussian Laser Beam Waist Size (in Pixels) for Log-Amplitude Variance Values of 0.1 – 0.5
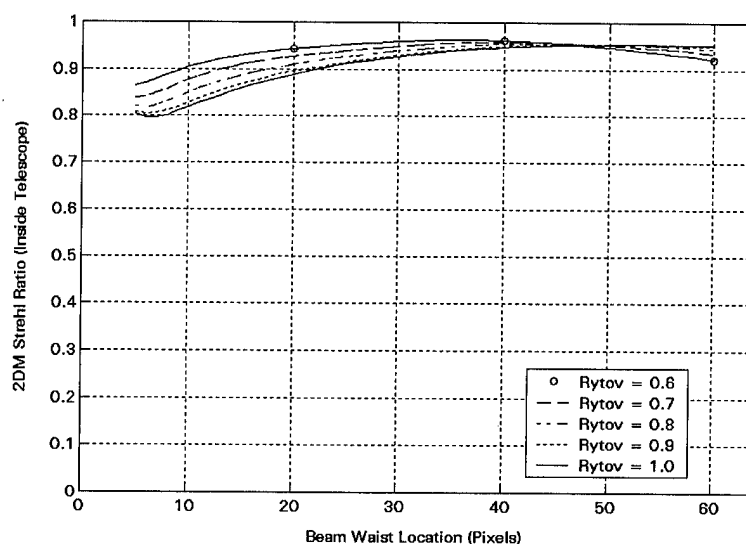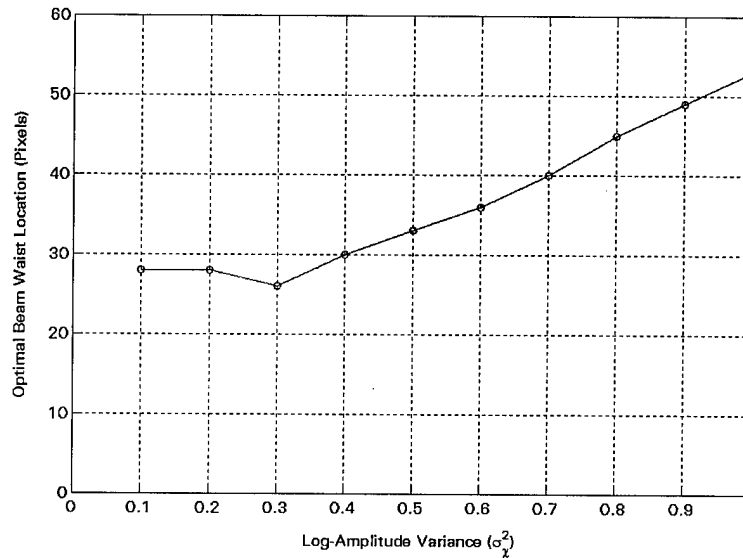

Figure 5.2. 2-DM Strehl Ratio (Inside Telescope) vs. Gaussian Laser Beam Waist Size (in Pixels) for Log-Amplitude Variance Values of 0.6 – 1.0

Figure 5.3. Optimal Gaussian Laser Beam Waist Size in the Plane of the Input Aperture vs. Log-Amplitude Variance

5.2 Strehl Ratio vs. the Conjugate Range of the 2nd DM

Using a beam waist of 28 pixels and a step-size of 2 km, the mean Strehl (over 32 realizations) is plotted versus the conjugate range of the second deformable mirror in Figure 5.4 and Figure 5.5. The conjugate range corresponding to maximum Strehl steadily decreases with increasing turbulence strength (Rytov parameter), which is clearly shown in Figure 5.6. This result seems non-intuitive at first glance; one would think that the opposite might be true because a greater propagation distance provides an increased ability of phase modulation at DM2 to modulate the amplitude profile at DM1. One possible explanation is that as the turbulence strength increases, the locations of regions of significant amplitude in the sensed beacon field vary to a greater extent. This effect requires a more severe modulation of the phase at DM2, which in turn increases the

5-4

energy loss due to the finite telescope aperture. The optimal range must therefore

decrease with increasing turbulence in order to overcome the energy loss. The impact of

energy loss due to the scattering caused by DM2 was first discussed by Roggemann [15].
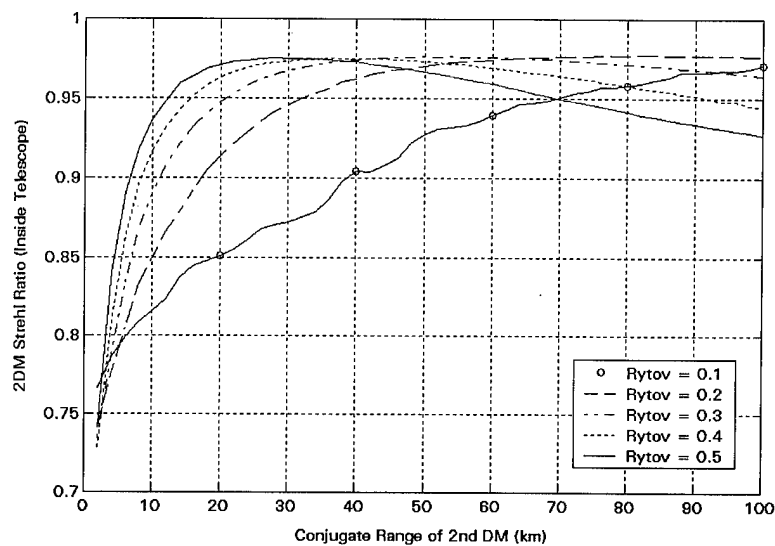
Figure 5.4. Mean 2-DM Strehl vs. the Conjugate Range of the 2nd DM for Log-Amplitude Variance Values of 0.1 through 0.5
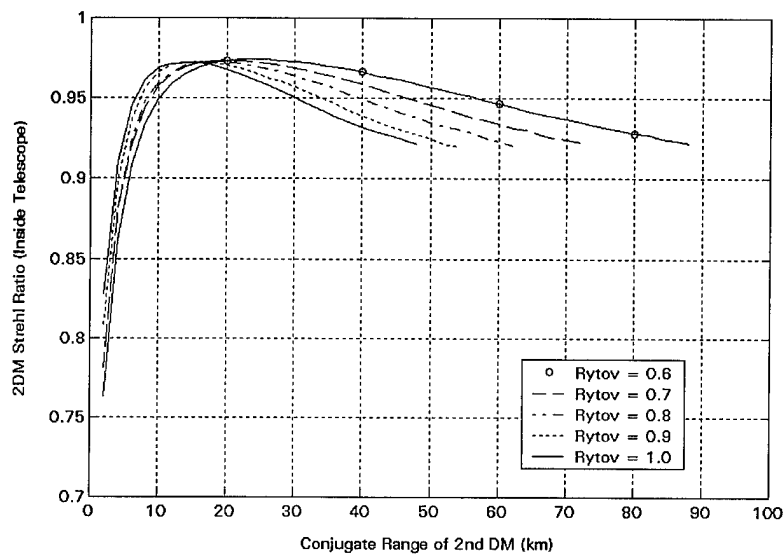
Figure 5.5. Mean 2 DM Strehl vs. the Conjugate Range of the 2nd DM for Log-Amplitude Variance Values of 0.6 through 1.0
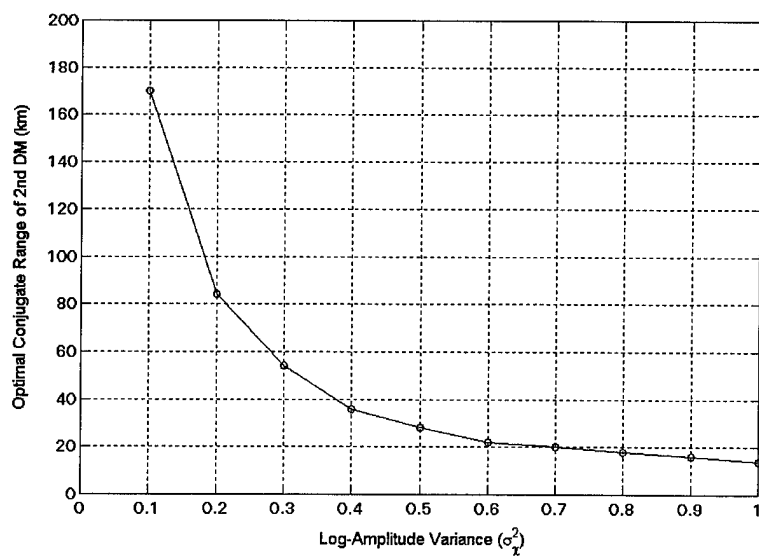
Figure 5.6. Optimal Conjugate Range of the 2nd DM vs. Log-Amplitude Variance

5.3 *Number of Branch Points vs. the Conjugate Range of the 2nd DM*

The conjugate range of DM2 corresponding to the maximum number of branch points in DM1 steadily decreases with increasing turbulence strength but saturates near 5 km for Rytov values of 0.5 and greater; see Figure 5.7 and Figure 5.8. The point of saturation resembles that of the actual Rytov versus theoretical Rytov shown in Figure 3.8. Initial inspection of Figure 5.9 and Figure 5.10 indicates a much larger number of branch points in DM2 versus DM1. The branch points in DM2, however, are counted over the entire propagation matrix whereas DM1 only contains branch points in a circular area 31 pixels in diameter; recall that DM1 is conjugate to the collecting aperture of the telescope (which acts as a mask on DM1 during iterations of the SGPA). The sudden jumps in the number of branch points in DM2 are due to the fact that the matrix dimension is allowed to jump from 128 x 128 pixels to 256 x 256 pixels when required to avoid propagator aliasing. The overall trend in the number of branch points in DM2 is decreasing with increasing conjugate range of DM2.
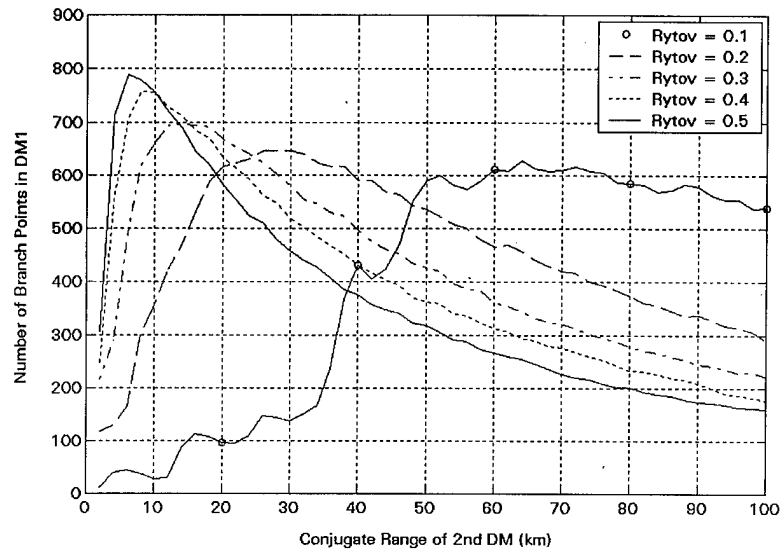
Figure 5.7. Mean Number of Branch Points in DM1 vs. the Conjugate Range of the 2nd DM for Log-Amplitude Variance Values of 0.1 through 0.5
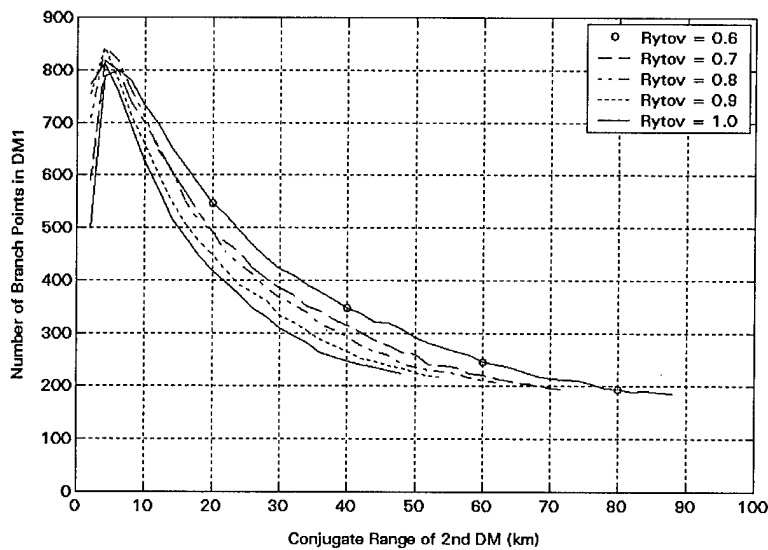
Figure 5.8. Mean Number of Branch Points in DM1 vs. the Conjugate Range of the 2nd DM for Log-Amplitude Variance Values of 0.6 through 1.0
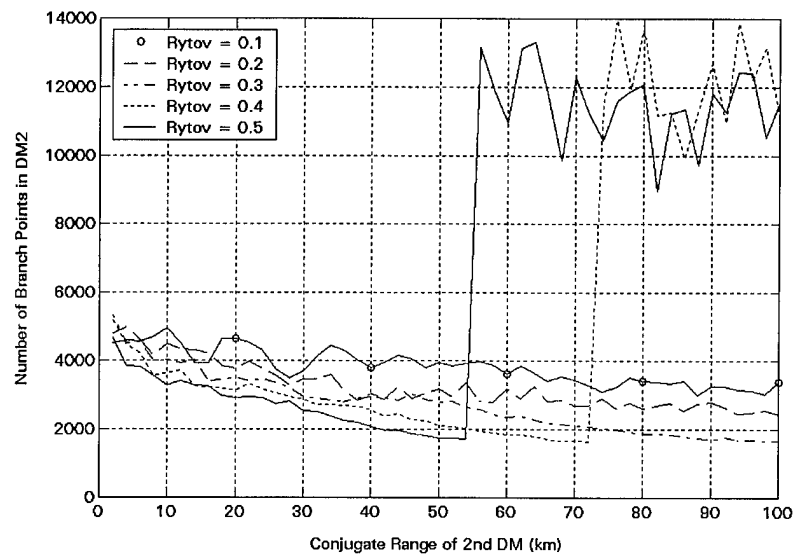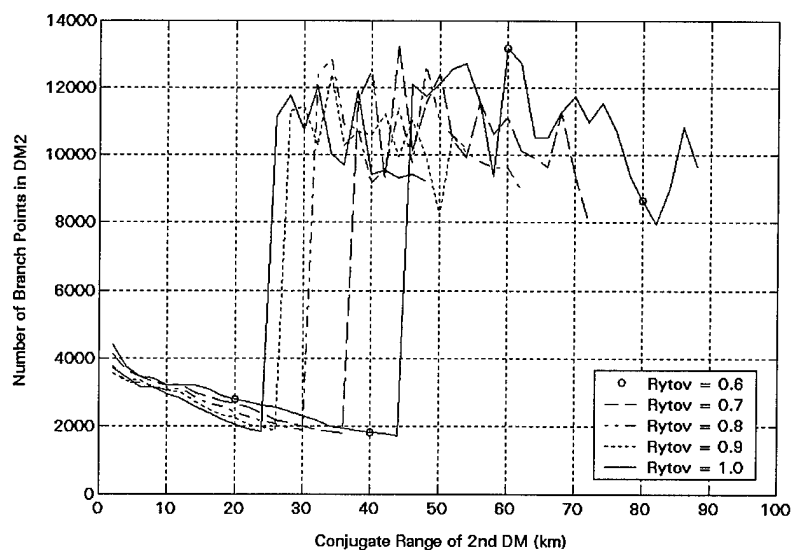
Figure 5.9. Mean Number of Branch Points in DM2 vs. the Conjugate Range of the 2nd DM for Log-Amplitude Variance Values of 0.1 through 0.5

Figure 5.10. Mean Number of Branch Points in DM2 vs. the Conjugate Range of the 2nd DM for Log-Amplitude Variance Values of 0.6 through 1.0

5.4 Number of Iterations to Convergence vs. the Conjugate Range of the 2nd DM

The mean number of iterations to convergence of the SGPA (to within 0.0005) is

plotted versus the conjugate range of the second DM in Figure 5.11 and Figure 5.12. The

peak number of iterations per Rytov value varies between approximately 60 and 80 and

the location of the peak decreases with increasing turbulence strength. The general

shapes of the curves are very similar to the shapes describing the number of branch points

in DM1; see Figure 5.7 and Figure 5.8. This would seem to indicate that a larger number

of SGPA iterations results in a larger number of branch points in DM1.
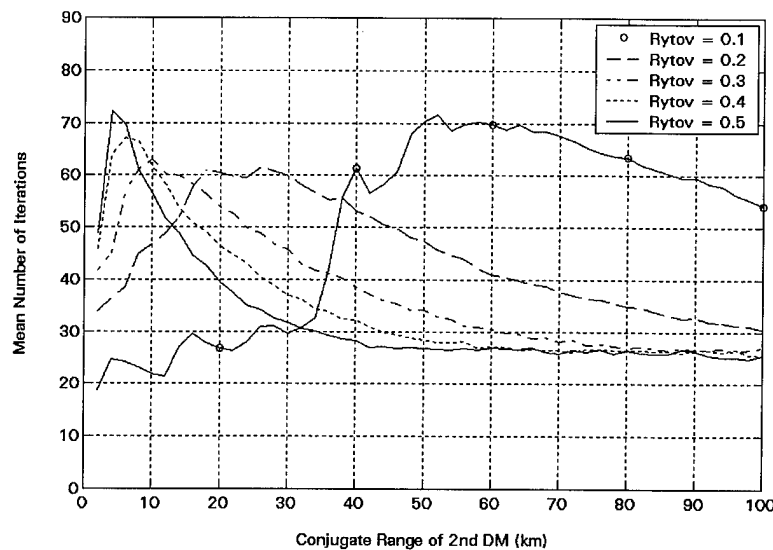
Figure 5.11. Mean Number of Iterations to Convergence vs. the Conjugate Range of the 2nd DM for Log-Amplitude Variance Values of 0.1 through 0.5
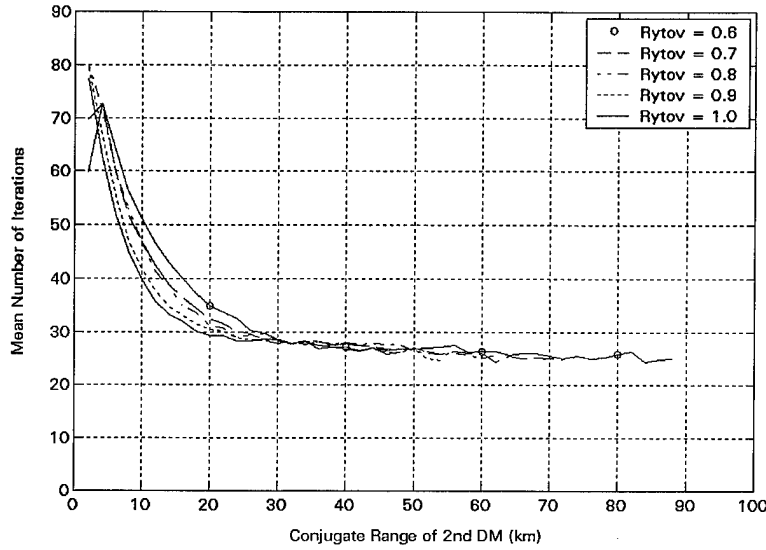
Figure 5.12. Mean Number of Iterations to Convergence vs. Conjugate Range of the 2nd DM for Log-Amplitude Variance Values of 0.6 through 1.0

5.5 Strehl Ratio vs. the Rytov Parameter

Using a finite input aperture of 31 pixels and a beam waist size (in the plane of the input aperture) of 28 pixels, the mean Strehl ratio is determined over an ensemble of 32 realizations for each value of the Rytov parameter. Both DMs are assumed to be "infinite" in size for this simulation. The conjugate range of the 2nd DM is set to 50 km except for the case of $\sigma_\chi^2 = 1.0$ in which a conjugate range of 48 km is used due to limited computing resources. To avoid propagator aliasing ranges greater than 48 km require a matrix size of 512 x 512 or greater for $\sigma_\chi^2 = 1.0$, which increases the required computing time significantly.

The Strehl ratios computed inside the telescope are plotted versus the Rytov parameter in Figure 5.13, including the 2-DM Strehl, 2-DM least squares Strehl, 1-DM

(i.e., phase only) Strehl, 1-DM least squares Strehl, and the uncompensated Strehl. For the Strehl ratios computed inside the telescope, the 2-DM Strehl remained above 0.9 for all values of log-amplitude variance. The performance of the 1-DM system gradually decreases from a Strehl of 0.75 to slightly less than 0.6 for Rytov values of 0.8 through 1.0.
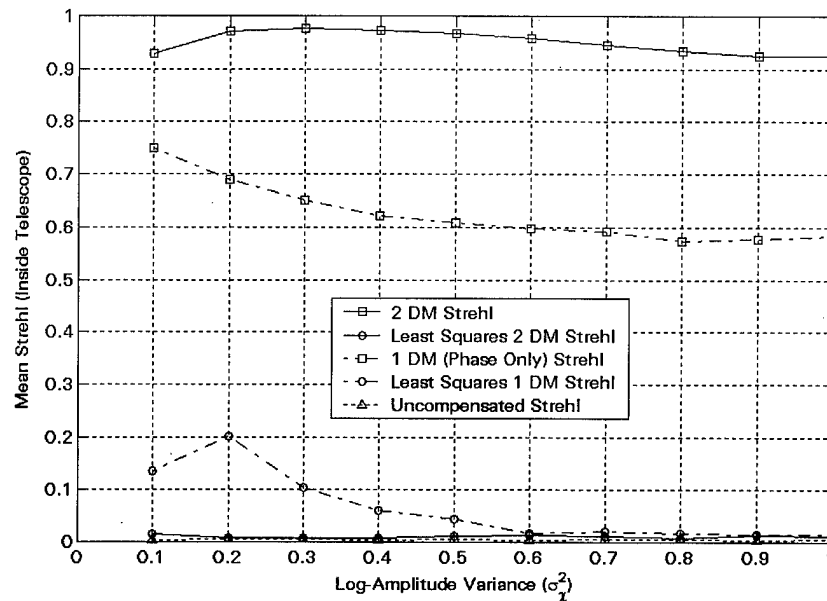

Figure 5.13. Mean Strehl Ratio Inside Telescope vs. Log-Amplitude Variance

In order to provide a more realistic evaluation of the performance of the 2 DM AO system, the Strehl ratio is also calculated outside the telescope by propagating the pre-compensated outgoing laser beam back through the original set of phase screens. This "back-propagated" Strehl is calculated in several ways (to provide increasing levels of realism) and is plotted in Figures 5.14 to 5.17.

First, the back-propagated Strehl is calculated using the original laser profile as the "ideal" field. Second, the laser field is propagated to the top of the atmosphere for use as the "ideal" field. Third, the laser is propagated to the telescope aperture, through the aperture, then to the top of the atmosphere. Finally, the most realistic approach is identical to the previous one with one exception; the Strehl ratio is penalized for energy lost due to the finite aperture. As expected, this last approach results in the lowest Strehl ratios. All 2-DM Strehl ratios calculated beyond the telescope, however, follow a similar trend and decrease monotonically with increasing turbulence strength. The system performance predicted by this assessment is significantly worse than that predicted by the in-telescope Strehls. However, even the most critical analysis indicates a performance increase of approximately 0.1 Strehl over the 1-DM system for the worst turbulence scenario.
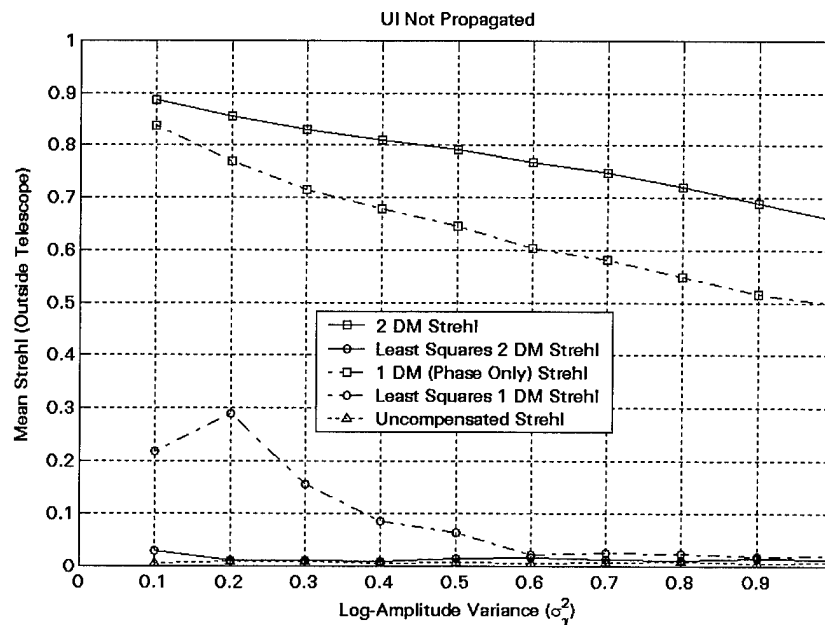
Figure 5.14. Mean Strehl Ratio Outside the Telescope vs. Log-Amplitude Variance
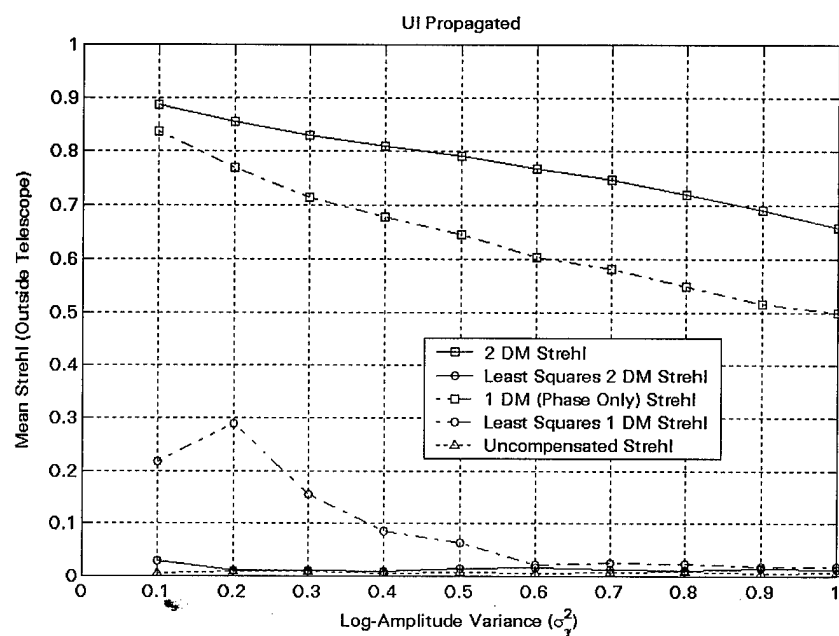
Figure 5.15. Mean Strehl Ratio Outside Telescope vs. Log-Amplitude Variance
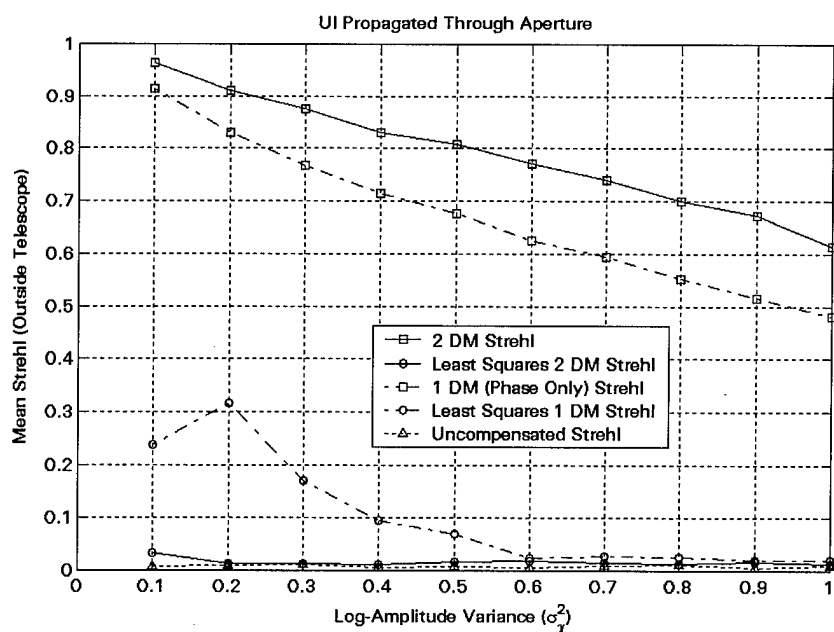
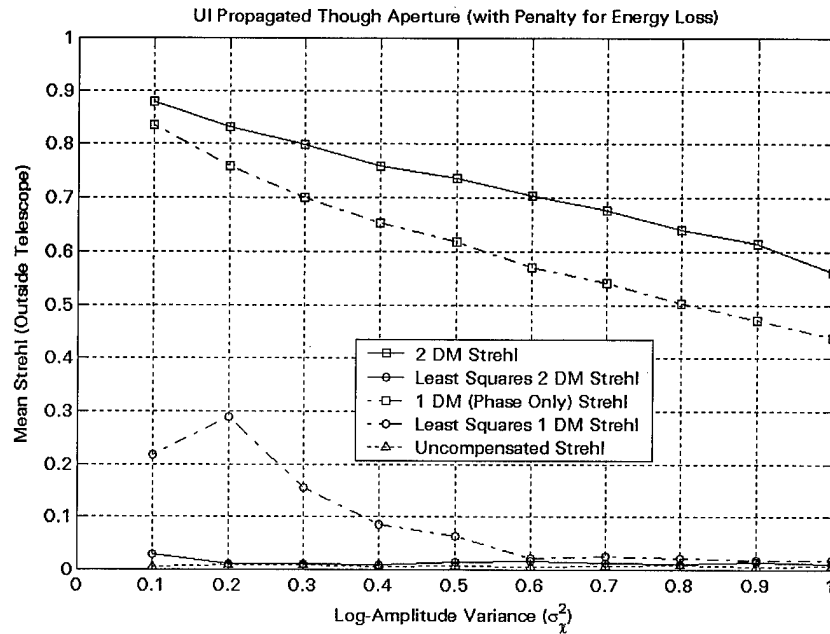**Figure 5.16. Mean Strehl Ratio Outside Telescope vs. Log-Amplitude Variance**

Figure 5.17. Mean Strehl Ratio Outside Telescope vs. Log-Amplitude Variance

Figures 5.18 to 5.22 plot the different Strehl ratios by type of AO system using both the in-telescope and beyond-telescope approaches. For all systems the first and second methods for calculating the Strehl ratio beyond the telescope yield nearly identical results. This result is not surprising given the fact that the Fourier transform of a Gaussian is another Gaussian. Furthermore, the divergence angle characterizing the Gaussian beam is not incorporated into this analysis.
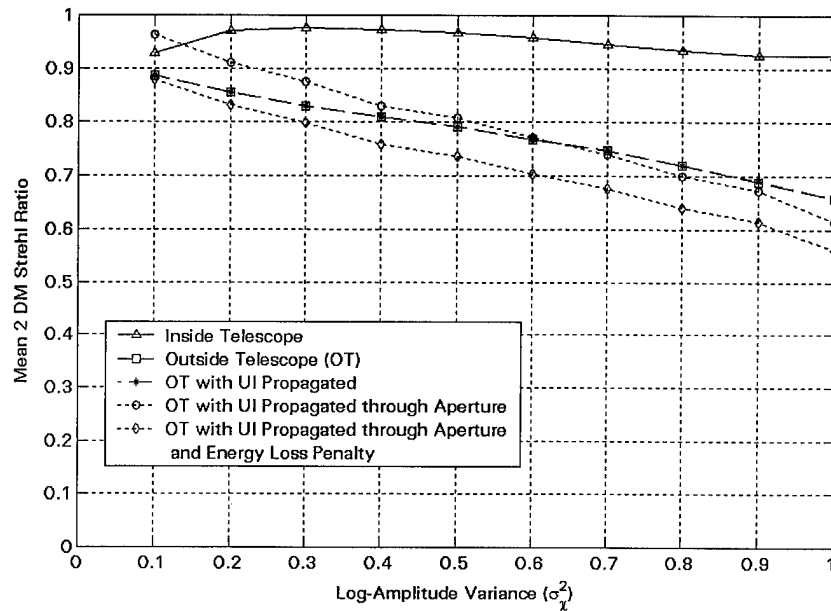
Figure 5.18. Mean 2-DM Strehl Ratio vs. Log-Amplitude Variance
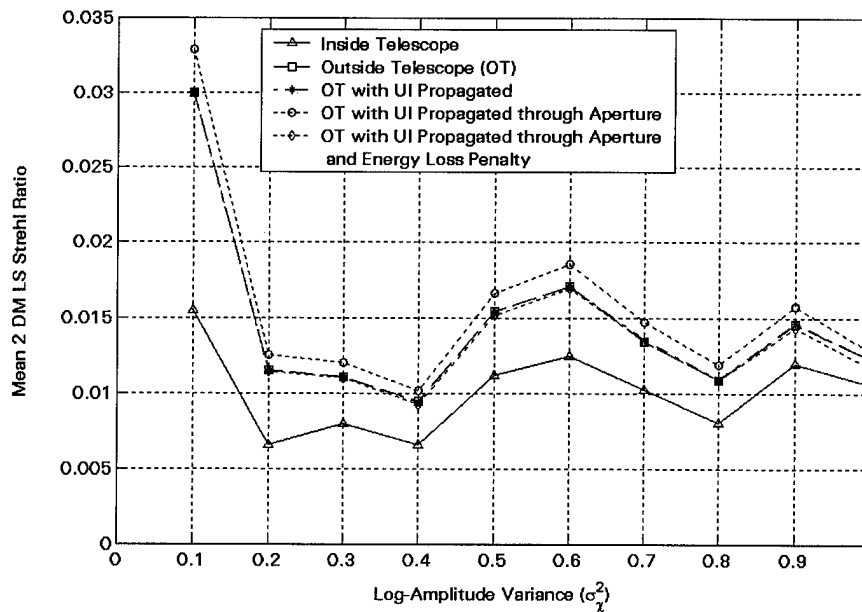
Figure 5.19. Mean Least Squares 2-DM Strehl Ratio vs. Log-Amplitude Variance
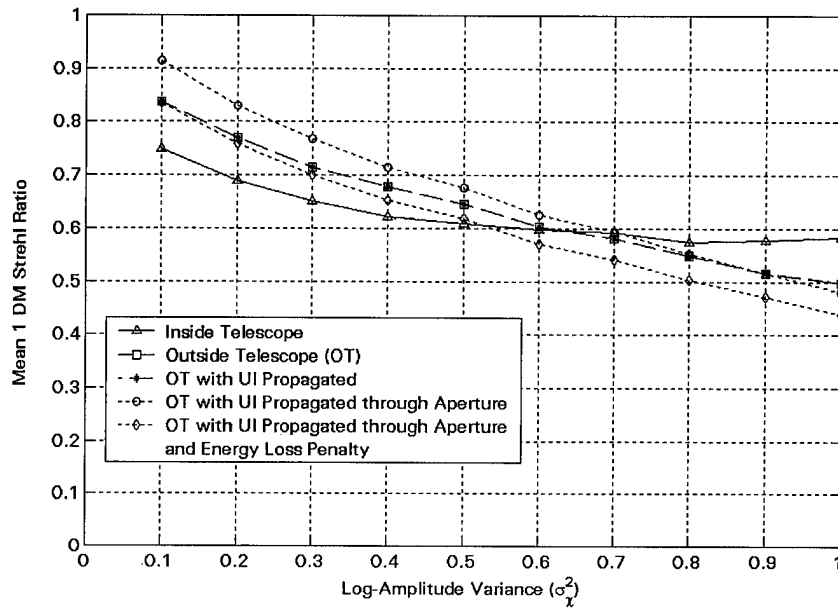
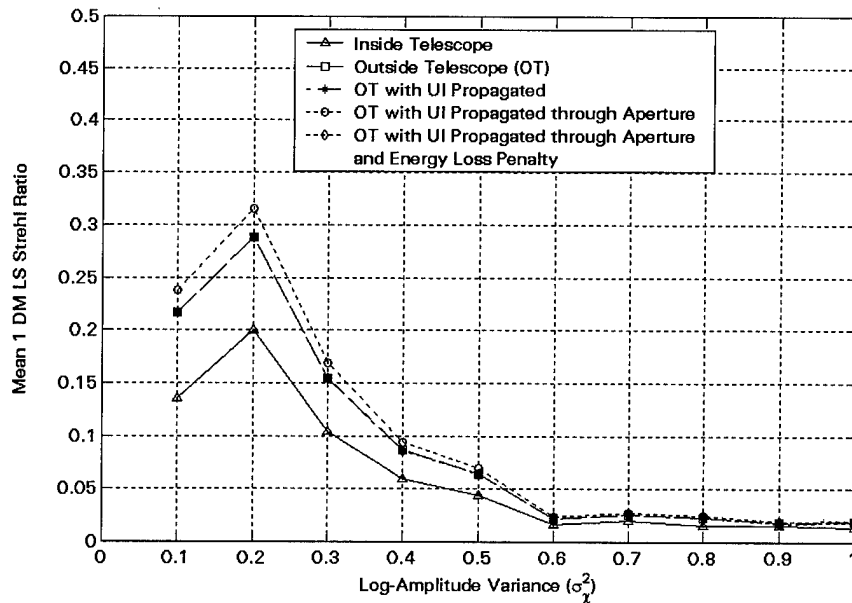**Figure 5.20. Mean 1-DM Strehl Ratio vs. Log-Amplitude Variance**

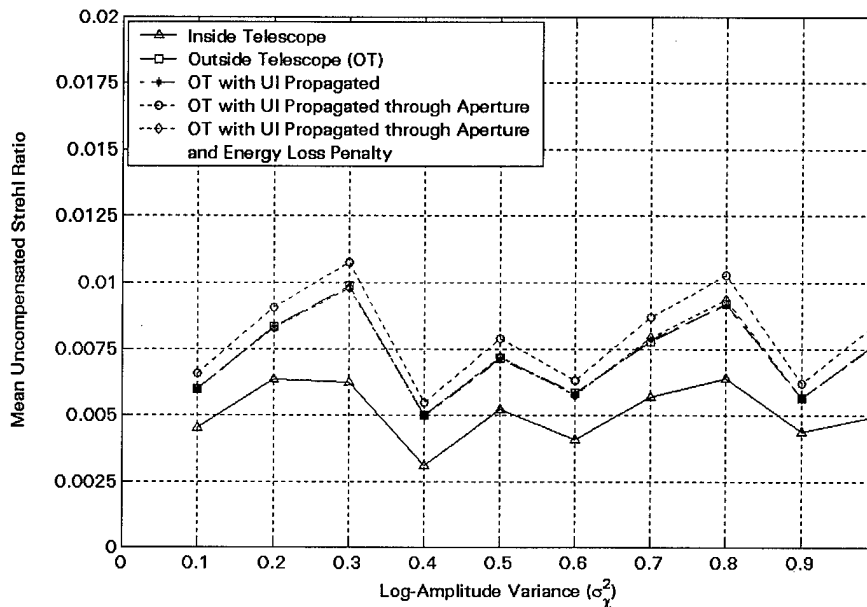**Figure 5.21. Mean Least Squares 1-DM Strehl Ratio vs. Log-Amplitude Variance**

Figure 5.22. Mean Uncompensated Strehl Ratio vs. Log-Amplitude Variance

5.6 Number of Branch Points vs. the Rytov Parameter

The numbers of branch points in each of the deformable mirror commands are plotted versus the log-amplitude variance in Figure 5.23 and Figure 5.24. The number of branch points in the beacon field or, conversely, in the 1-DM system mirror commands are plotted versus Rytov parameter in Figure 5.25. The number of branch points in the DM1 commands for the 2-DM system is nearly 600 branch points for the weakest turbulence, but decreases to about 240 branch points for Rytov values of 0.9 and 1.0. The numbers of branch points in the DM2 commands are orders of magnitude greater for log-amplitude variance values above 0.5. Once again, this is due to counting branch points over a larger grid; a 256 x 256 pixel propagation matrix is required for Rytov values

5-18

greater than or equal to 0.6 and propagation distances greater than or equal to 50 km. Furthermore, the branch points in the DM1 commands are effectively limited to the area within a circular aperture of radius equal to 31 pixels due to the fact that DM1 is conjugate to the collecting aperture of the telescope. The large numbers of branch points explains the extremely poor performance (only slightly better than uncompensated) of the least squares 2-DM system, as seen in Figure 5.19. The hidden phase for these numbers of branch points clearly contains a significant portion of the information for the DM controls. The relatively small number of branch points in the 1-DM system mirror commands (i.e., beacon field) is one reason that phase-only correction is able to maintain significant performance increases over an uncompensated system even at the worst turbulence strengths.
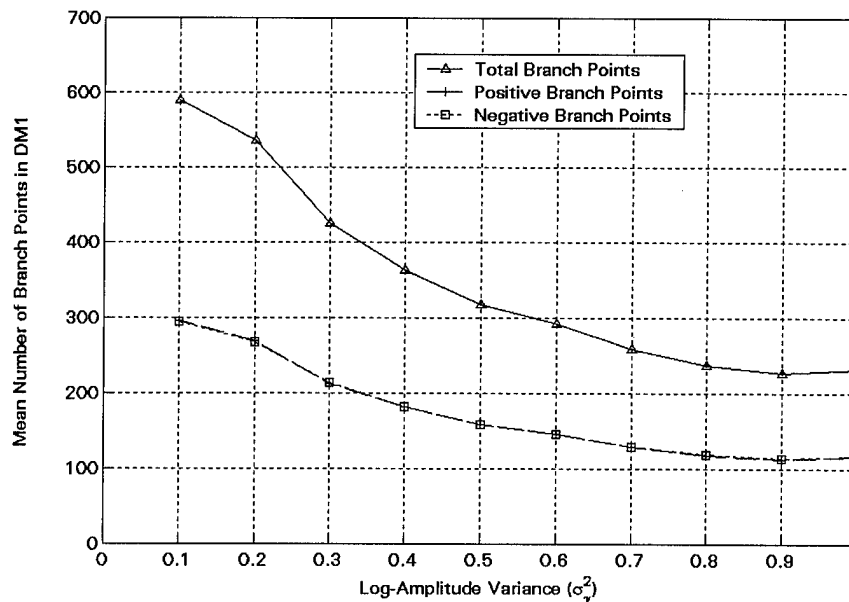
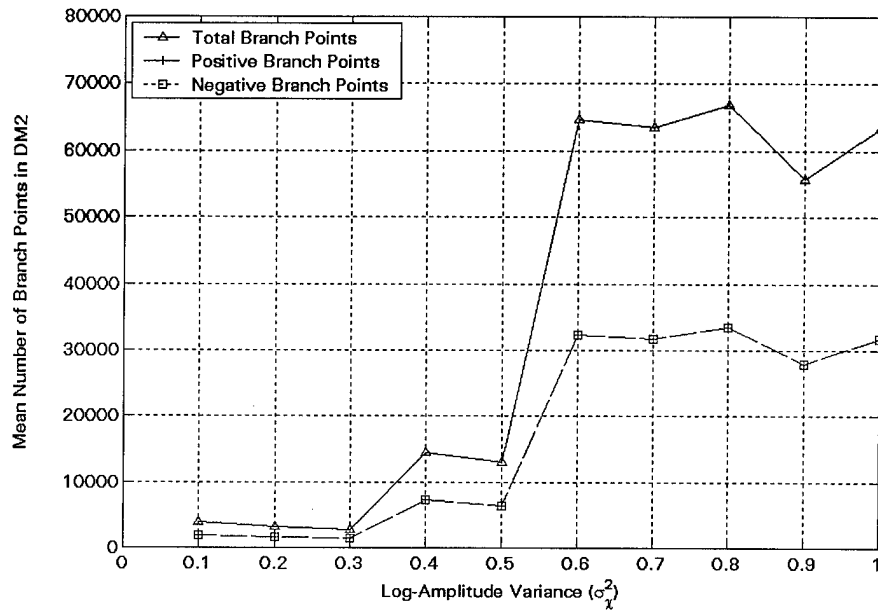Figure 5.23. Mean Number of Branch Points in DM1 vs. Log-Amplitude Variance

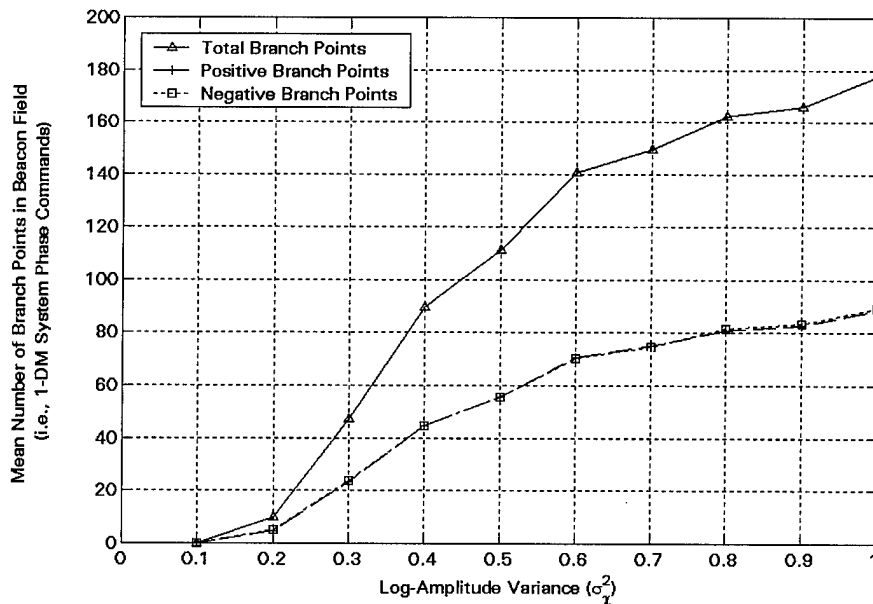**Figure 5.24. Mean Number of Branch Points in DM2 vs. Log-Amplitude Variance**

Figure 5.25. Mean Number of Branch Points in Beacon Field (i.e., 1-DM System Mirror Commands) vs. Log-Amplitude Variance

5.7 Number of Iterations to Convergence vs. the Rytov Parameter

The number of iterations of the SGPA algorithm required to converge to within 0.0005 Strehl decreases rapidly with increasing Rytov parameter up to a Rytov value of 0.5; see Figure 5.26. The saturation of the required iterations near 27 occurs at about σ_χ^2 = 0.5, which roughly corresponds to the value of theoretical Rytov past which a saturation in measured Rytov (see Figure 3.8) occurs. The decrease in required iterations may be due to the fact that as scintillation becomes worse there is less integrated amplitude in the beacon field (to which the SGPA must reshape the Gaussian laser beam against).
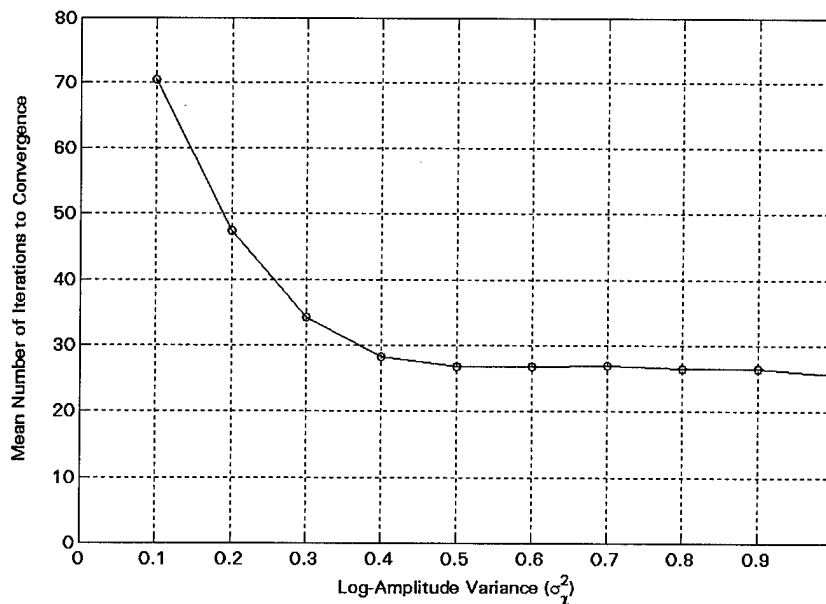

Figure 5.26. Mean Number of Iterations to SGPA Convergence vs. Log-Amplitude Variance

5.8 Strehl Ratio vs. the Radii of the Deformable Mirrors

To model the impact of energy loss (due to finite DM size) on the Strehl ratio, the radii of both DMs are varied simultaneously. This is accomplished in two ways: 1) by masking the field (not just the phase), which is analogous to forming a finite mirror for which the entire surface is deformable and 2) by masking the phase, which is analogous to forming an infinite flat surface mirror for which only a finite center portion is deformable. A real system would probably mask the phase (i.e., use a large DM but only control a central section). However, the results presented here indicate only a very minor difference in Strehl for the two approaches. Both approaches are used to plot the 2-DM Strehl, the least squares 2-DM Strehl, the 1-DM Strehl, and the least squares 1-DM Strehl in Figure 5.27 for a Rytov value of 0.1. The results are so similar, in fact, that only the first (most conservative) approach is used for the remaining simulations in this section.
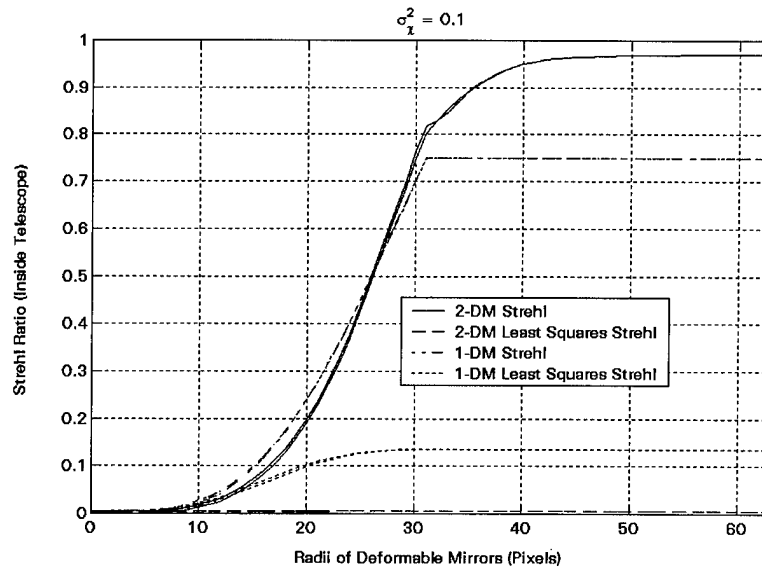

Figure 5.27. Strehl Ratio (Inside Telescope) vs. Radii of the Deformable Mirrors for a Log-Amplitude Variance of 0.1

The SGPA is run once for each beacon field realization per Rytov value, and thus the subsequent Strehl ratios (for a given beacon field realization) are all calculated with one set of phase commands with varying mirror sizes. The results are plotted in Figures 5.28 to 5.37. As expected, the Strehl of the 1-DM system reaches an absolute maximum as the radius of the single DM equals the radius of the input aperture. This outcome is due to the fact that the 1-DM system can only impact the outgoing field in the plane of the telescope's collecting aperture. The 2-DM system, however, achieves a significant increase in Strehl for DM radii that increase beyond the size of the input aperture. This result also makes sense due to the fact that phase modulations at any point in the outgoing field in the plane of DM2 can affect the amplitude of the field at (theoretically) any other point in the field after propagation to DM1.
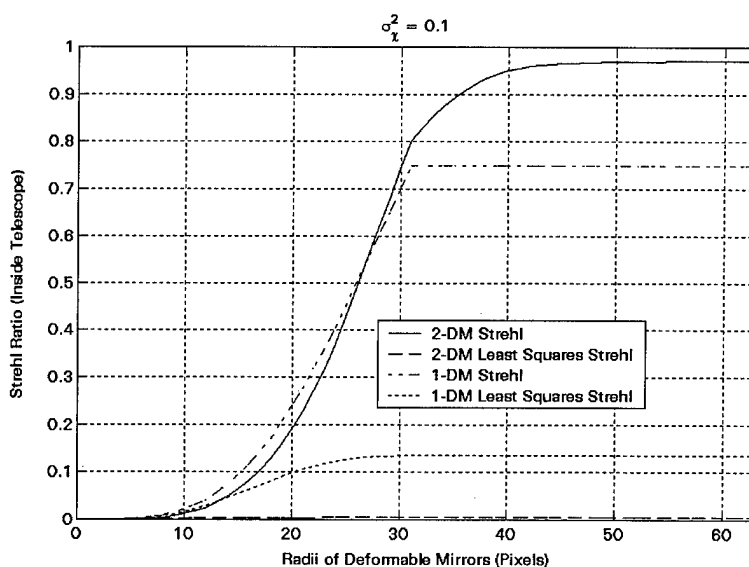

Figure 5.28. Strehl Ratio (Inside Telescope) vs. Radii of the Deformable Mirrors for a Log-Amplitude Variance of 0.1
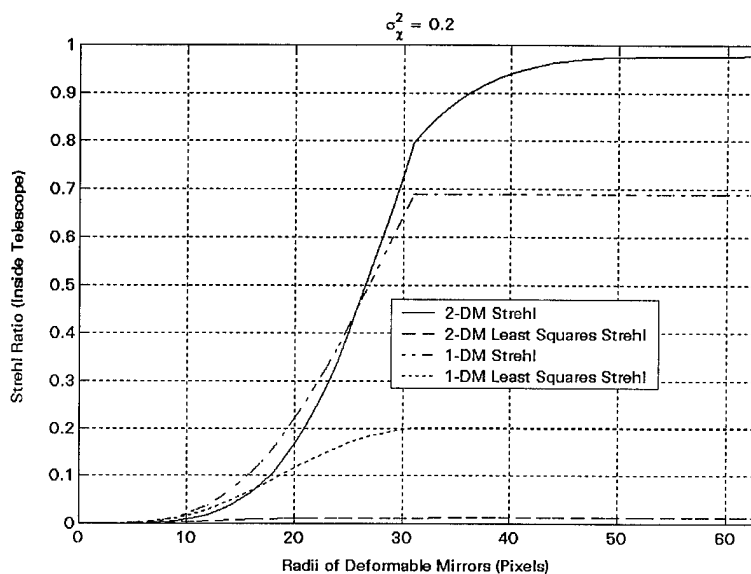
Figure 5.29. Strehl Ratio (Inside Telescope) vs. Radii of the Deformable Mirrors for a Log-Amplitude Variance of 0.2
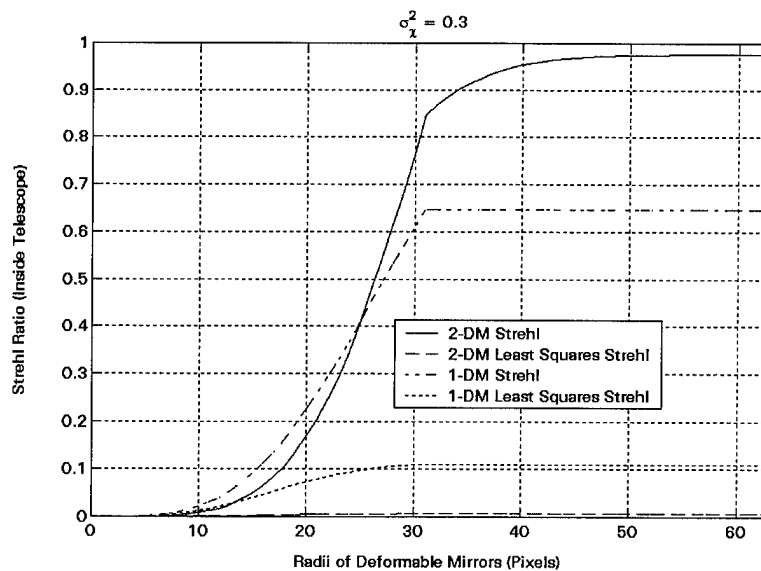

Figure 5.30. Strehl Ratio (Inside Telescope) vs. Radii of the Deformable Mirrors for a Log-Amplitude Variance of 0.3
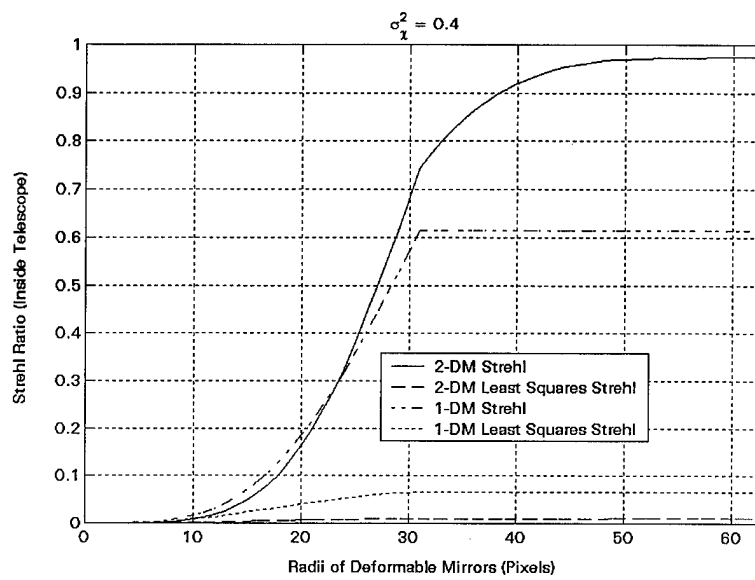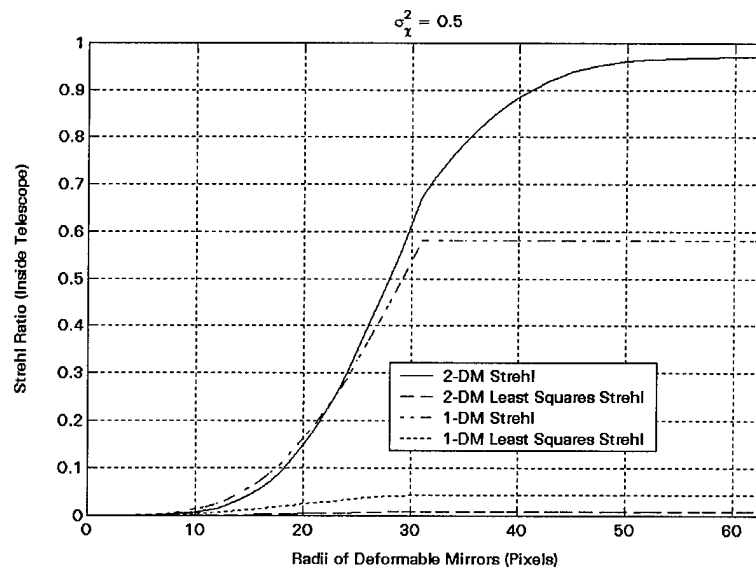
5-24

Figure 5.31. Strehl Ratio (Inside Telescope) vs. Radii of the Deformable Mirrors for a Log-Amplitude Variance of 0.4

Figure 5.32. Strehl Ratio (Inside Telescope) vs. Radii of the Deformable Mirrors for a Log-Amplitude Variance of 0.5
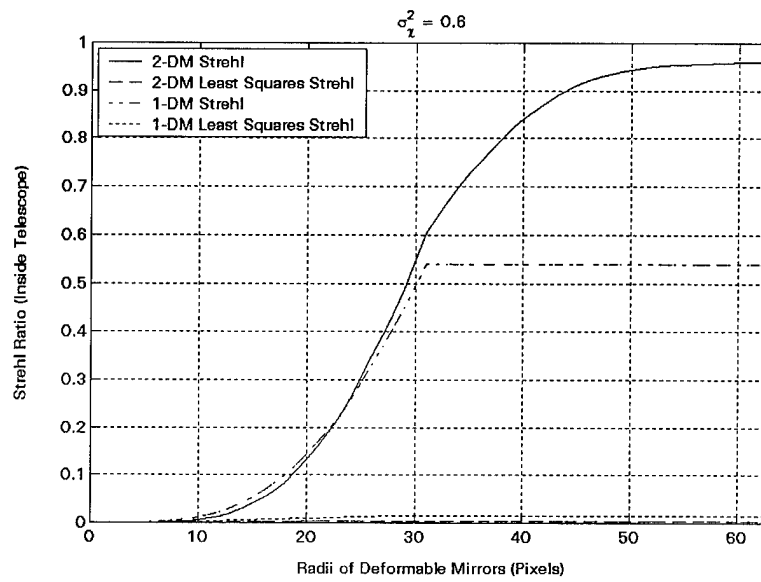
Figure 5.33. Strehl Ratio (Inside Telescope) vs. Radii of the Deformable Mirrors for a Log-Amplitude Variance of 0.6
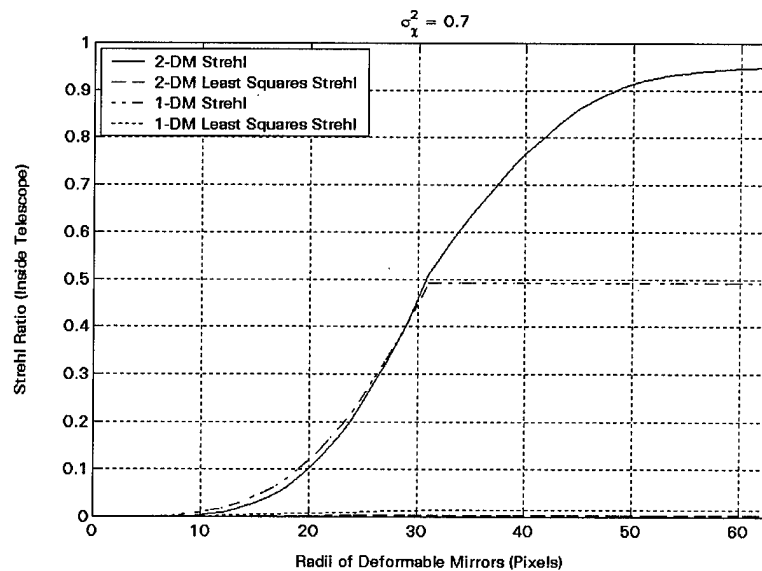

Figure 5.34. Strehl Ratio (Inside Telescope) vs. Radii of the Deformable Mirrors for a Log-Amplitude Variance of 0.7
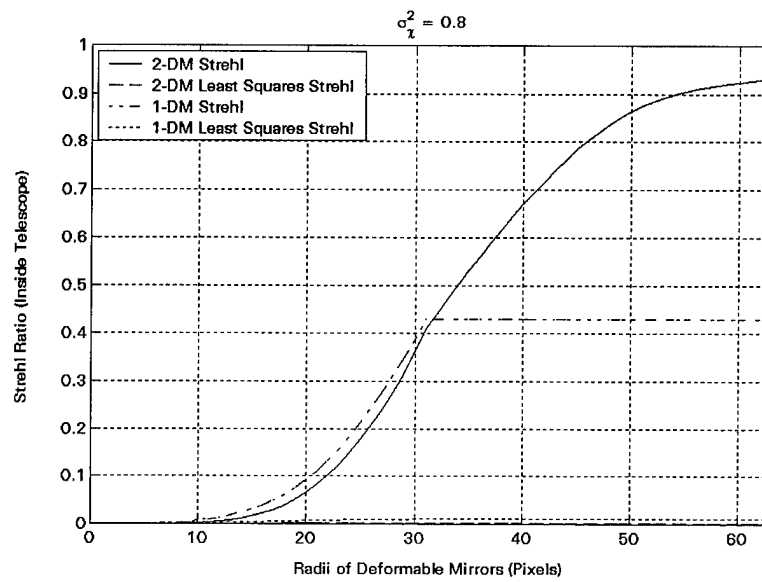
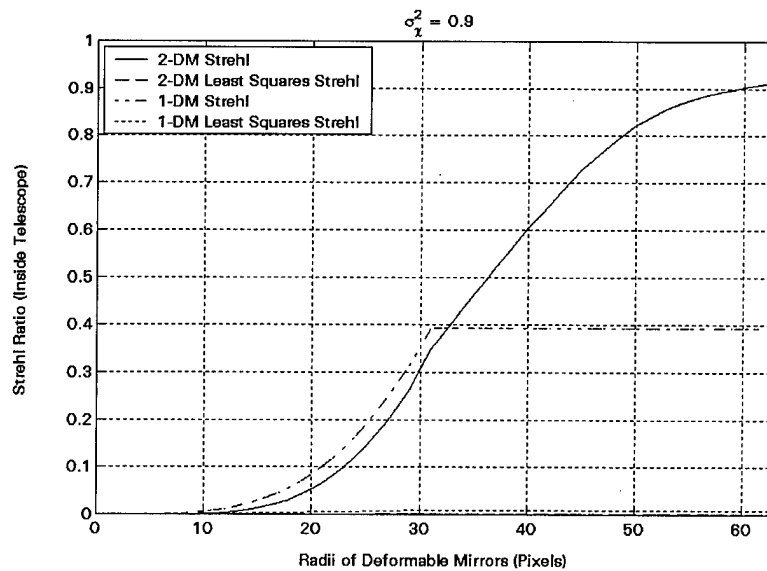**Figure 5.35. Strehl Ratio (Inside Telescope) vs. Radii of the Deformable Mirrors for a Log-Amplitude Variance of 0.8**

Figure 5.36. Strehl Ratio (Inside Telescope) vs. Radii of the Deformable Mirrors for a Log-Amplitude Variance of 0.9
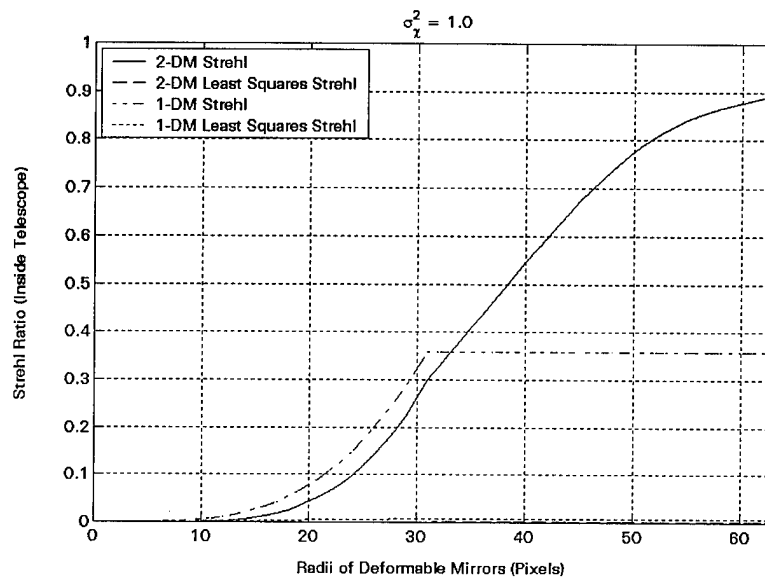
$\sigma_\chi^2 = 1.0$

Strehl Ratio (Inside Telescope)

2-DM Strehl
2-DM Least Squares Strehl
1-DM Strehl
1-DM Least Squares Strehl

Radii of Deformable Mirrors (Pixels)

Figure 5.37. Strehl Ratio (Inside Telescope) vs. Radii of the Deformable Mirrors for a Log-Amplitude Variance of 1.0

5.9 Number of Branch Points vs. the Radii of the Deformable Mirrors

The numbers of branch points in each of the DMs is plotted versus log-amplitude variance in Figures 5.38 to 5.47. As with the phase-only correction system, the numbers of branch points in the controls for DM1 reach an absolute maximum at DM radii equal to and greater than that of the input aperture. This result is due to the fact that the first deformable mirror can only effect the phase of the outgoing laser in the area limited by the collecting aperture of the telescope. This fact is expressed mathematically in the SGPA phase iterative update equation for DM1 commands in Equation (4.6). The numbers of branch points in the commands for DM2 undergo a sharp increase for radii near 45 pixels for all levels of turbulence strength.
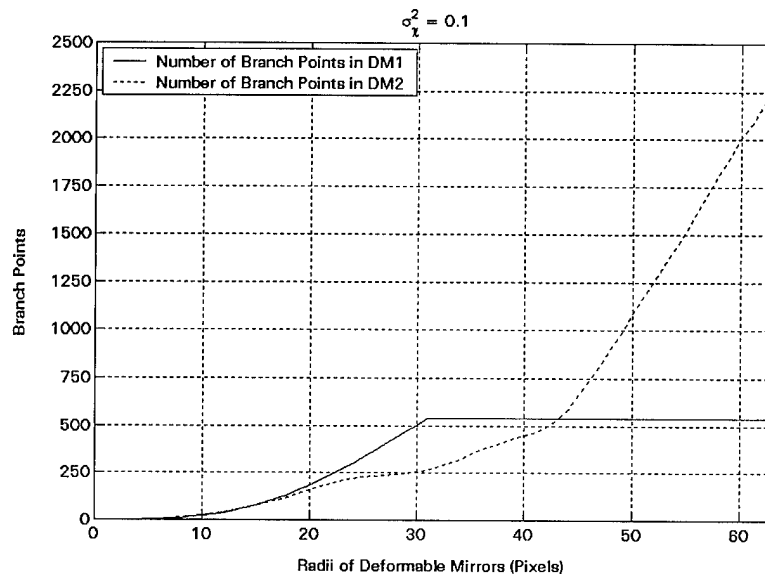
5-28

Figure 5.38. Number of Branch Points in 2-DM Commands vs. Radii of DMs for a Log-Amplitude Variance of 0.1

Figure 5.39. Number of Branch Points in 2-DM Commands vs. Radii of DMs for a Log-Amplitude Variance of 0.2

$$\sigma_\chi^2 = 0.3$$

Figure 5.40. Number of Branch Points in 2-DM Commands vs. Radii of DMs for a Log-Amplitude Variance of 0.3

$$\sigma_\chi^2 = 0.4$$

Figure 5.41. Number of Branch Points in 2-DM Commands vs. Radii of DMs for a Log-Amplitude Variance of 0.4

5-30
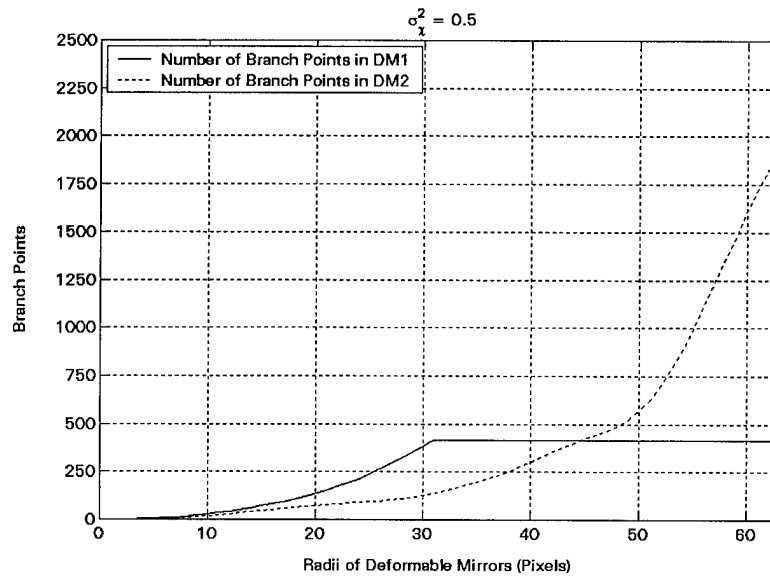
Figure 5.42. Number of Branch Points in 2-DM Commands vs. Radii of DMs for a Log-Amplitude Variance of 0.5
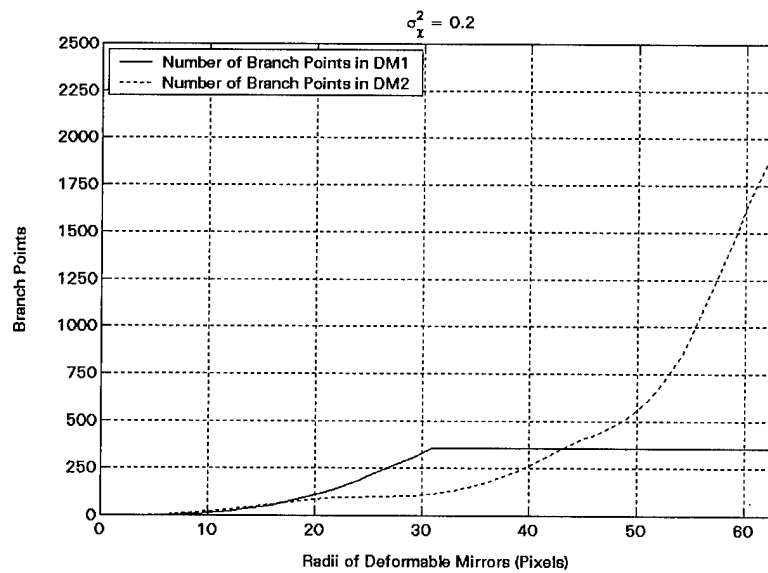

Figure 5.43. Number of Branch Points in 2-DM Commands vs. Radii of DMs for a Log-Amplitude Variance of 0.6
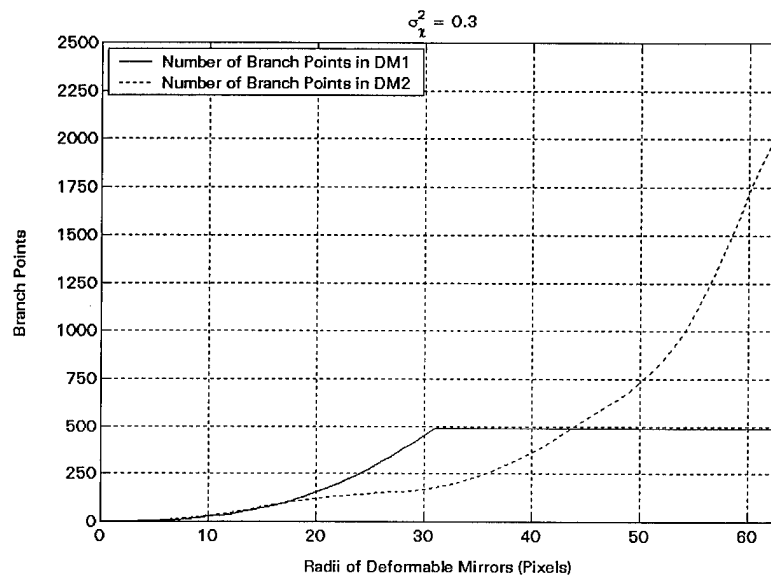
Figure 5.44. Number of Branch Points in 2-DM Commands vs. Radii of DMs for a Log-Amplitude Variance of 0.7

Figure 5.45. Number of Branch Points in 2-DM Commands vs. Radii of DMs for a Log-Amplitude Variance of 0.8
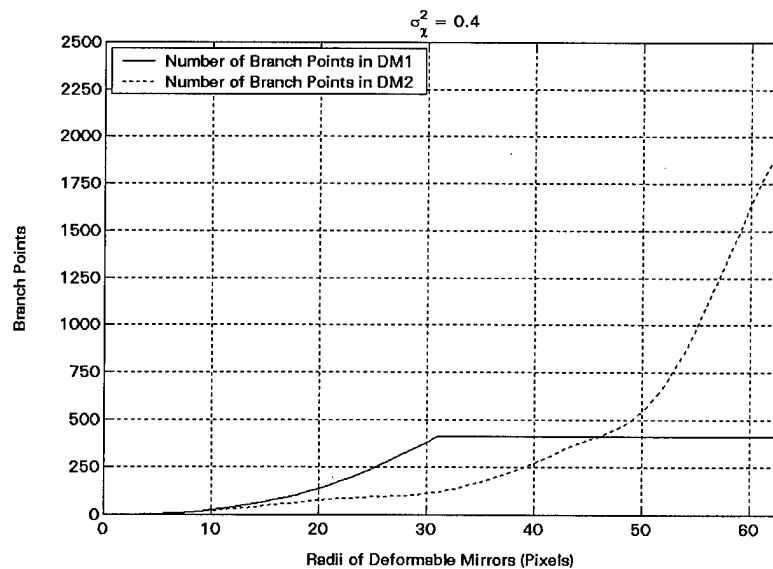
Figure 5.46. Number of Branch Points in 2-DM Commands vs. Radii of DMs for a Log-Amplitude Variance of 0.9

Figure 5.47. Number of Branch Points in 2-DM Commands vs. Radii of DMs for a Log-Amplitude Variance of 1.0
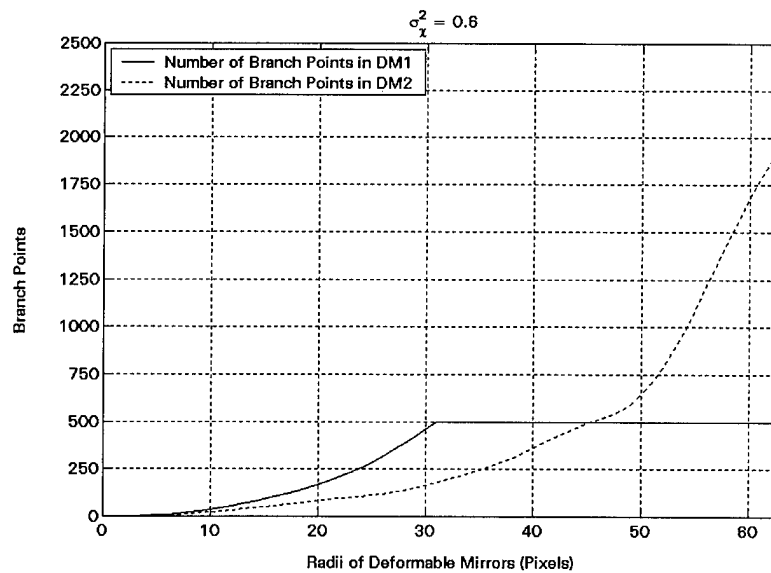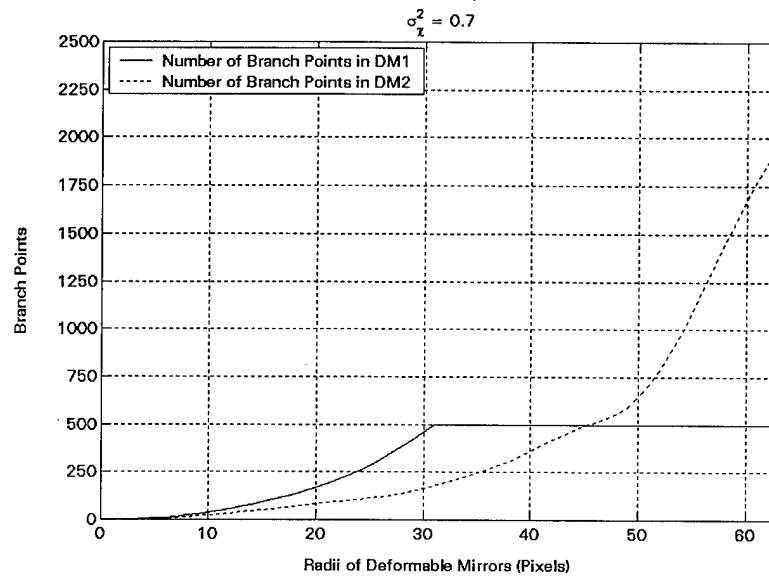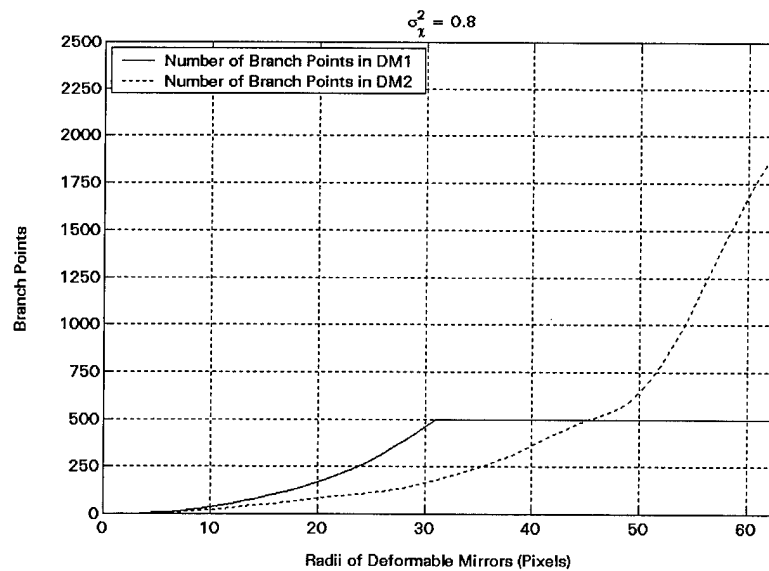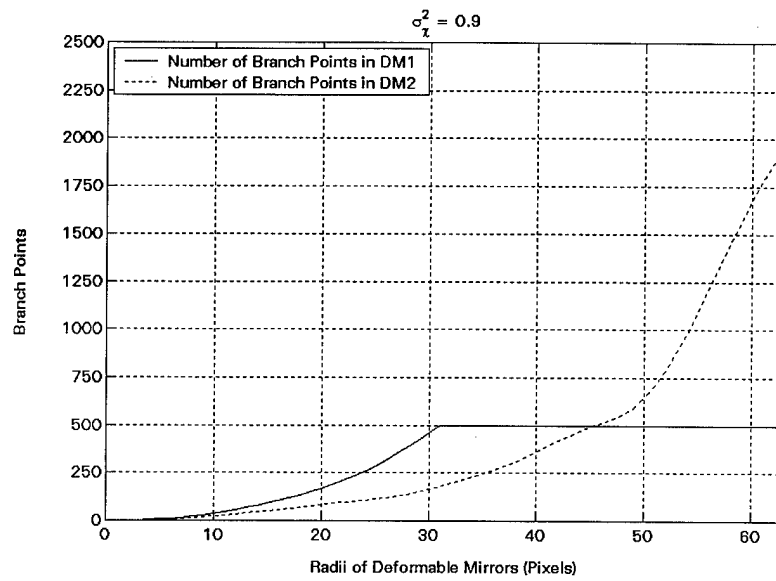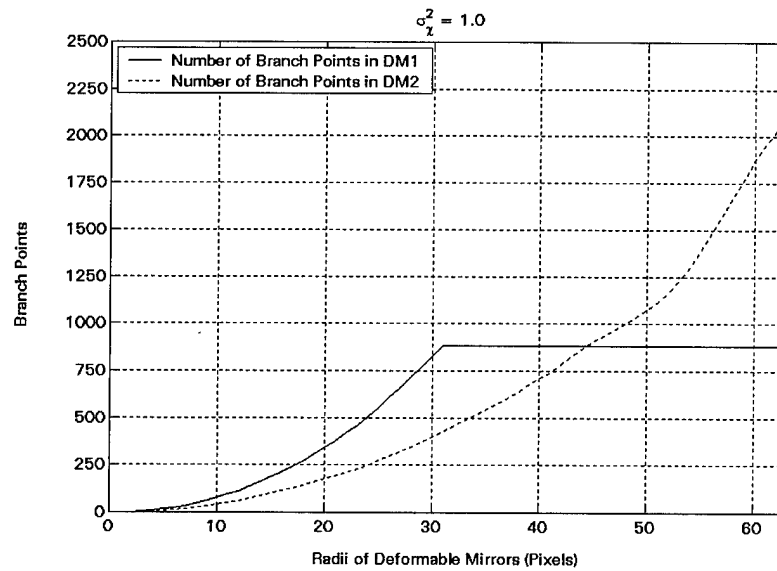
6. Conclusions and Recommendations

The addition of a second deformable mirror to the two-DM AO transmission system clearly improves theoretical performance (over a single DM system) for delivering energy on target through atmospheric turbulence. Strehl ratios calculated by back-propagating the modulated laser beam through the atmosphere, however, indicate a less significant improvement over the single DM system (compared to Strehl ratios calculated inside the telescope).

The hidden phase contained in the branch points is critical to the performance of the SGPA, as indicated by the two-DM least squares Strehl ratio results. The DM commands generated by the SGPA are corrupted by a large number of branch points, and this problem has at least two possible solutions. One solution is the use of a phase reconstruction scheme other than least squares, and another solution is the use of a new two-DM algorithm that imposes constraints on the number of branch points in the DM commands. An effective real-world solution will probably combine both approaches, and work is underway toward this end.

Allowing the conjugate range of DM2 to be finite minimizes the energy lost at DM1 due to scattering caused by the phase modulation at DM2. For this reason the two-DM system with the second DM conjugate to a finite range should outperform the system with the second DM conjugate to the far-field (infinity).

Recommendations for further research are provided below.

6-1

First, track computing time per SGPA iteration. Such tracking could be done for all of the analyses accomplished in this thesis, with the final result being an average number of seconds per iteration.

Second, perform the Strehl versus Gaussian beam waist size optimization with the inclusion of a penalty to the Strehl ratio calculation for energy in the Gaussian laser beam lost (i.e., unaccounted for) outside the finite propagation matrix.

Third, execute the Strehl versus DM radii analysis while keeping track of the amount of energy lost outside the finite DMs. The amount of lost energy should increase with decreasing DM size and with increasing turbulence strength. Similarly, the Strehl versus conjugate range of DM2 analysis could be accomplished while keeping track of the amount of energy lost outside of DM1. The energy lost will most likely increase with increasing conjugate range of DM2 and increasing turbulence strength.

Finally, complete the number of branch points in DM2 versus both Rytov value and the conjugate range of DM2 analyses while constraining the area within which branch points are counted to the size of the finite collecting aperture of the telescope. This extension would provide a basis for fair comparison of the number of branch points in DM1 with the number of branch points in DM2, due to the fact that the numbers of branch points in DM1 are inherently counted only within an area equal to the size of the collecting aperture, as DM1 is conjugate to that plane. Another approach would be to normalize the number of branch points to some unit area. The locations of branch points could also be investigated. It has been reported in the literature that branch points tend to occur more often in regions of lower intensity [12].

In summary, the more critical Strehl ratio analysis performed by back-propagating the pre-compensated laser beam through the atmospheric models indicates that a two-DM AO system provides increased performance over that of a one-DM system. Accounting for the hidden phase contained in the branch points corrupting the mirror commands (produced by the SGPA algorithm), however, is critical to successful implementation of the SGPA.

Appendix A. Fields Used for Testing SGPA Algorithm

Figure A.1. Intensity Plot of One Realization for a Log-Amplitude Variance of 0.1

Figure A.2. Intensity Plot of One Realization for a Log-Amplitude Variance of 0.2

Figure A.3. Intensity Plot of One Realization for a Log-Amplitude Variance of 0.3
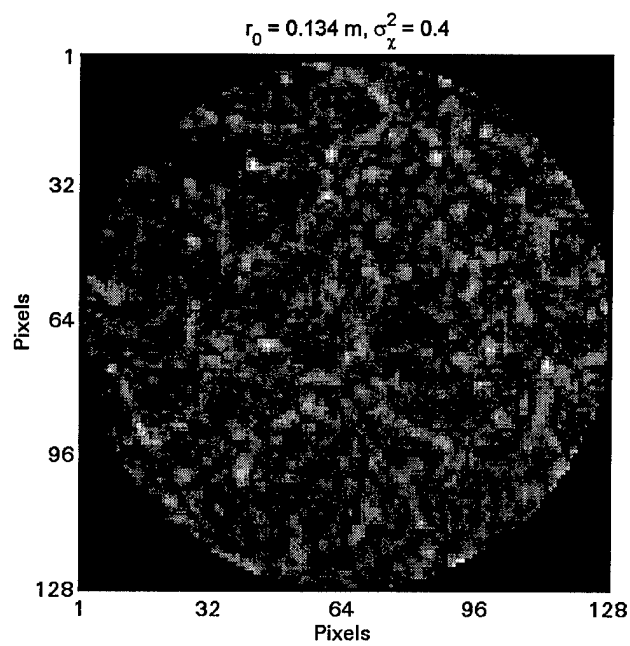
Figure A.4. Intensity Plot of One Realization for a Log-Amplitude Variance of 0.4
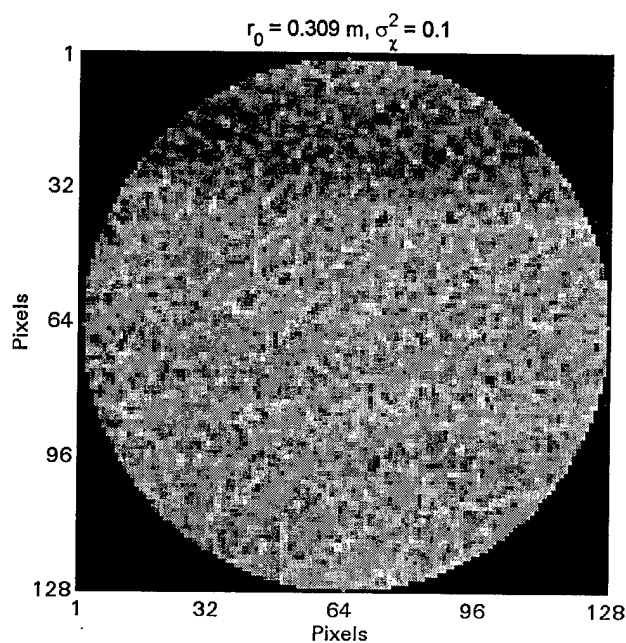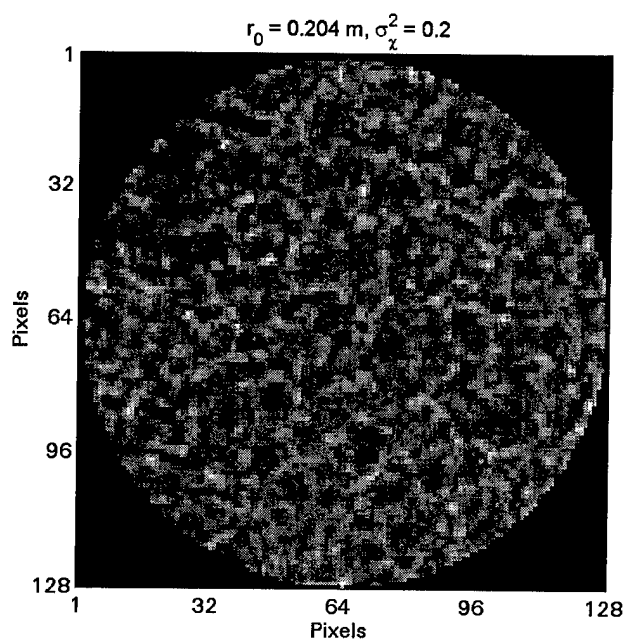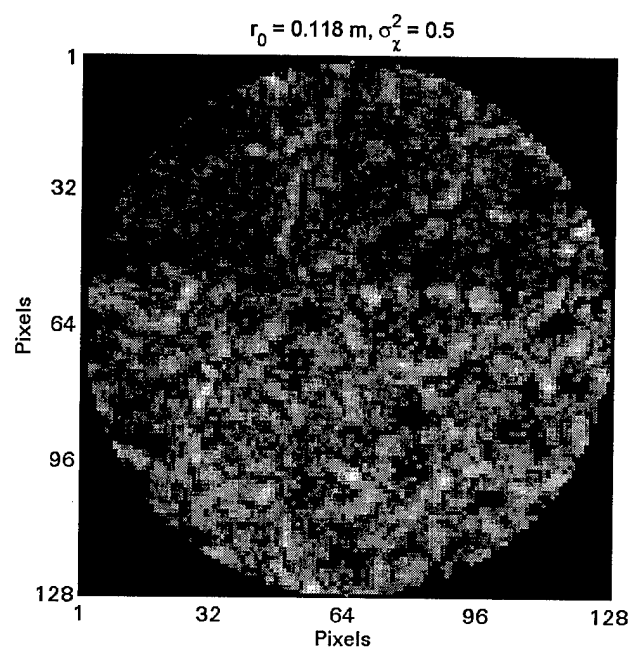
Figure A.5. Intensity Plot of One Realization for a Log-Amplitude Variance of 0.5
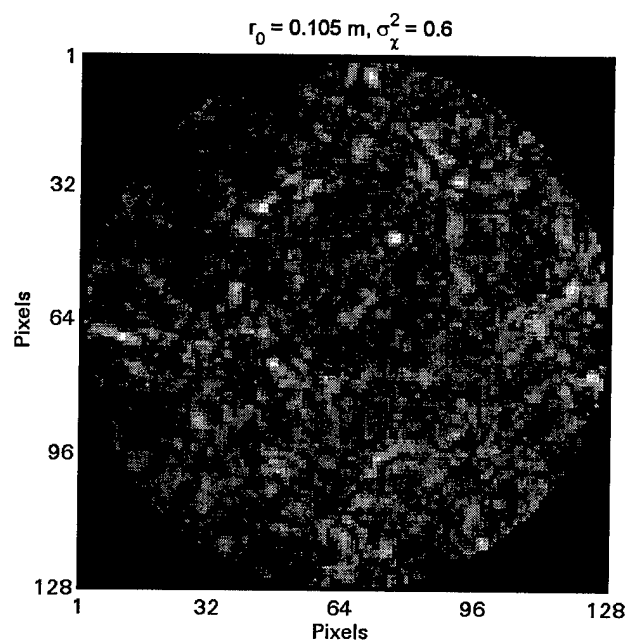
Figure A.6. Intensity Plot of One Realization for a Log-Amplitude Variance of 0.6

A-3

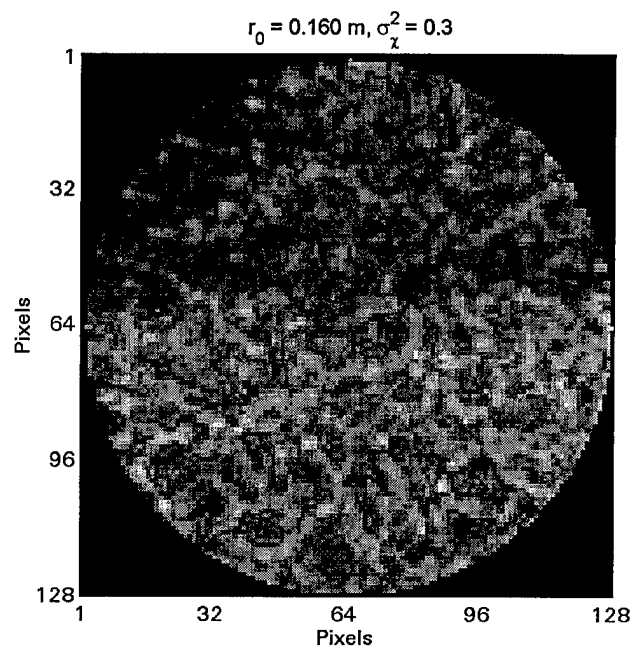$r_0 = 0.096$ m, $\sigma_\chi^2 = 0.7$
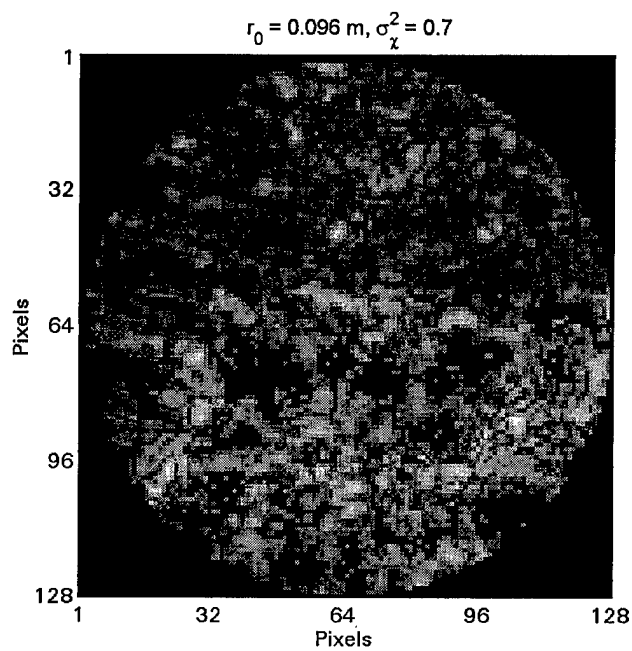
Figure A.7. Intensity Plot of One Realization for a Log-Amplitude Variance of 0.7

$r_0 = 0.089$ m, $\sigma_\chi^2 = 0.8$
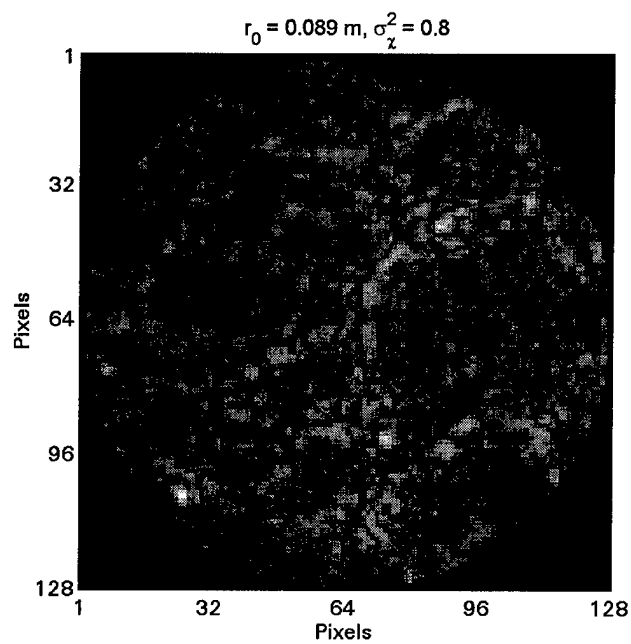
Figure A.8. Intensity Plot of One Realization for a Log-Amplitude Variance of 0.8

A-4

$r_0 = 0.083$ m, $\sigma_\chi^2 = 0.9$
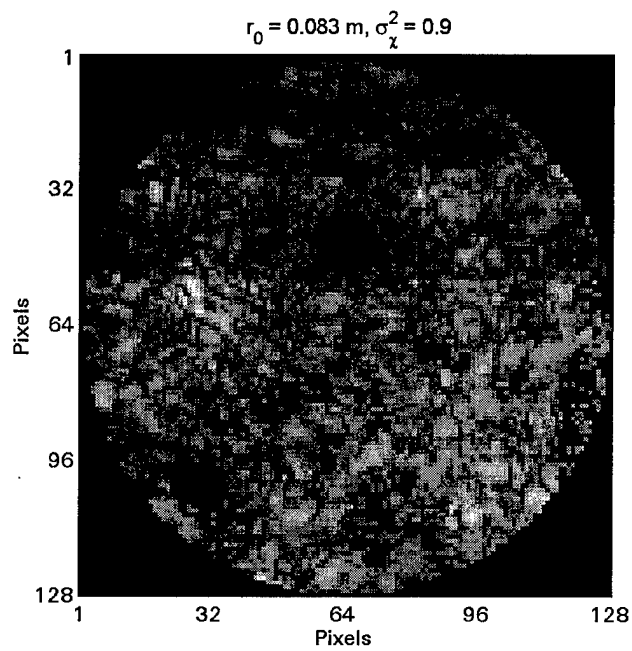
Figure A.9. Intensity Plot of One Realization for a Log-Amplitude Variance of 0.9

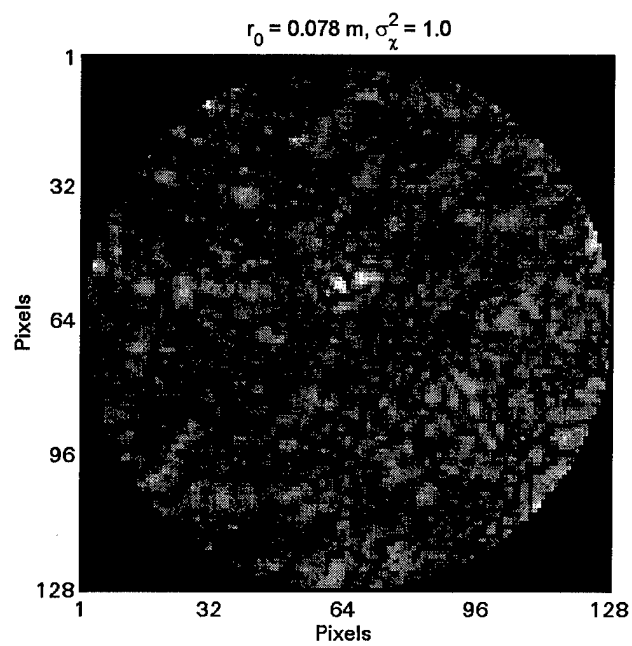
$r_0 = 0.078$ m, $\sigma_\chi^2 = 1.0$

Figure A.10. Intensity Plot of One Realization for a Log-Amplitude Variance of 1.0

Bibliography

[1]   L. A. Thompson, "Adaptive Optics in Astronomy," *Physics Today*, pp. 24-31, 1994.

[2]   M. C. Roggemann and D. J. Lee, "Two-deformable-mirror concept for correcting scintillation effects in laser beam projection through the turbulent atmosphere," *Applied Optics*, vol. 37, pp. 4577-4585, 1998.

[3]   R. J. Noll, "Zernike polynomials and atmospheric turbulence," *Journal of the Optical Society of America*, vol. 66, pp. 207-211, 1976.

[4]   R. K. Tyson, *Principles of Adaptive Optics*, 2nd ed. Boston: Academic Press Limited, 1998.

[5]   F. G. Smith, "Atmospheric Propagation of Radiation," in *The Infrared and electro-optical systems handbook*, vol. 2, J. S. Accetta and D. L. Shumaker, Eds. Ann Arbor, Mich. Bellingham, Wash.: Infrared Information Analysis Center ; SPIE Optical Engineering Press, 1993, pp. 321.

[6]   D. L. Fried, "Optical Resolution Through a Randomly Inhomogeneous Medium," *Journal of the Optical Society of America*, vol. 56, pp. 1372-1379, 1966.

[7]   V. I. Tatarski, "The Effects of the Turbulent Atmosphere on Wave Propagation," U.S. Department of Commerce, Springfield, VA NOAA Report No. TT 68-50464, 1972.

[8]   M. C. Roggemann and B. M. Welsh, *Imaging through turbulence*: CRC Press, 1996.

[9]   B. L. McGlamery, "Computer Simulation Studies of Compensation of Turbulence Degraded Images," *SPIE/OSA*, vol. 74, pp. 225-233, 1976.

[10]   R. G. Lane, Glindermann, A., Dainty, J. C., "Simulation of a Kolmolgorov Phase Screen," *Waves in Random Media*, vol. 2, pp. 209-224, 1992.

[11]   B. L. Ellerbroek, "Notes on MCAO Using Angular Spectrum Propagator," , 1998.

[12]   J. D. Barchers and B. L. Ellerbroek, "Improved compensation of turbulence-induced amplitude and phase distortions by means of multiple near-field phase adjustments," *to be submitted to The Journal of the Optical Society of America*, 2000.

[13] D. L. Fried, "Branch Point Problem in Adaptive Optics," *Journal of the Optical Society of America A*, vol. 15, pp. 2759-2768, 1998.

[14] J. T. Verdeyen, *Laser Electronics*, Third ed. Englewood Cliffs, NJ: Prentice Hall, 1995.

[15] M. C. Roggemann and S. Deng, "Scintillation compensation for laser beam projection using segmented deformable mirrors," presented at Propagation and Imaging through the Atmosphere III, Denver, CO, 1999.

REPORT DOCUMENTATION PAGE		*Form Approved* *OMB No. 0704-0188*

The public reporting burden for this collection of information is estimated to average 1 hour per response, including the time for reviewing instructions, searching existing data sources, gathering and maintaining the data needed, and completing and reviewing the collection of information. Send comments regarding this burden estimate or any other aspect of this collection of information, including suggestions for reducing the burden, to Department of Defense, Washington Headquarters Services, Directorate for Information Operations and Reports (0704-0188), 1215 Jefferson Davis Highway, Suite 1204, Arlington, VA 22202-4302. Respondents should be aware that notwithstanding any other provision of law, no person shall be subject to any penalty for failing to comply with a collection of information if it does not display a currently valid OMB control number. **PLEASE DO NOT RETURN YOUR FORM TO THE ABOVE ADDRESS.**

1. REPORT DATE *(DD-MM-YYYY)* xx-03-2000	2. REPORT TYPE Master's Thesis	3. DATES COVERED *(From - To)* Sep 1999 - Mar 2000

4. TITLE AND SUBTITLE	5a. CONTRACT NUMBER N/A
Multi-Conjugate Adaptive Optics for the Compensation of Amplitude and Phase Distortions	5b. GRANT NUMBER N/A
	5c. PROGRAM ELEMENT NUMBER N/A
6. AUTHOR(S) Crabtree, Peter N.	5d. PROJECT NUMBER N/A
	5e. TASK NUMBER N/A
	5f. WORK UNIT NUMBER N/A

7. PERFORMING ORGANIZATION NAME(S) AND ADDRESS(ES) Air Force Institute of Technology Graduate School of Engineering and Management (AFIT/EN) 2950 P Street, Building 640 WPAFB, OH 45433-7765	8. PERFORMING ORGANIZATION REPORT NUMBER AFIT/GEO/ENG/00M-01

9. SPONSORING/MONITORING AGENCY NAME(S) AND ADDRESS(ES) AFRL/DES Attn: Maj David J. Lee 3550 Aberdeen Ave SE Kirtland AFB, NM 87117 Commercial: 505-846-5822 or DSN: 246-5822	10. SPONSOR/MONITOR'S ACRONYM(S) N/A
	11. SPONSOR/MONITOR'S REPORT NUMBER(S) N/A

12. DISTRIBUTION/AVAILABILITY STATEMENT

APPROVED FOR PUBLIC RELEASE; DISTRIBUTION UNLIMITED

13. SUPPLEMENTARY NOTES
Thesis Advisor: Dr. Steven C. Gustafson, ENG
Commercial: 937-255-3636 ext. 4598 or DSN: 785-3636 ext. 4598

14. ABSTRACT
Two deformable mirrors (DMs) with finite conjugate ranges are investigated for compensating amplitude and phase distortions due to laser propagation through turbulent atmospheres. Simulations are performed based on Adaptive Optics (AO) for an Airborne Laser-type scenario. The Strehl ratio, the number of branch points in DM controls, and the number of iterations to convergence are used as figures of merit to evaluate performance of the Sequential Generalized Projection Algorithm that generates mirror commands. The results are ensemble averages over 32 realizations of the scintillated test fields for each value of the Rytov parameter within the test scenario. The Gaussian beam shape that optimizes the Strehl ratio is determined. The least squares two-DM Strehl, phase-only Strehl, least squares phase-only Strehl, and uncompensated Strehl are also determined for comparison. Finally, for the Strehl ratio versus Rytov parameter analysis the Strehl is also calculated beyond the telescope by propagating the pre-compensated laser wavefront back through the phase screens of the modeled atmosphere. Results from the more critical beyond-telescope Strehl analysis indicate that a two-DM AO system provides an increase in performance of approximately 0.1 in Strehl as compared to the phase-only system for the most severe simulated turbulence (theoretical log-amplitude variance of 1.0).

15. SUBJECT TERMS
Adaptive Optics, Multi-Conjugate Adaptive Optics, Strehl Ratio, Branch Points, Atmospheric Turbulence, Laser Propagation, Energy Projection, Sequential Generalized Projection Algorithm

16. SECURITY CLASSIFICATION OF:			17. LIMITATION OF ABSTRACT	18. NUMBER OF PAGES	19a. NAME OF RESPONSIBLE PERSON Dr. Steven C. Gustafson
a. REPORT U	b. ABSTRACT U	c. THIS PAGE U	SAR	102	19b. TELEPHONE NUMBER *(Include area code)* Commercial: 937-255-2024 or DSN: 785-2024

Standard Form 298 (Rev. 8/98)
Prescribed by ANSI Std. Z39.18